Monthly Notices
of the
ROYAL ASTRONOMICAL SOCIETY

MNRAS **492,** 1869–1886 (2020)
Advance Access publication 2019 December 20

doi:10.1093/mnras/stz3575

Decoupling the rotation of stars and gas – I. The relationship with morphology and halo spin

Christopher Duckworth [1,2★] Rita Tojeiro [1] and Katarina Kraljic[3]

[1] *School of Physics and Astronomy, University of St Andrews, North Haugh, St Andrews, KY16 9SS, UK*
[2] *Center for Computational Astrophysics, Flatiron Institute, 162 Fifth Avenue, New York, NY 10010, USA*
[3] *Institute for Astronomy, University of Edinburgh, Royal Observatory, Blackford Hill, Edinburgh EH9 3HJ, UK*

Accepted 2019 December 16. Received 2019 December 11; in original form 2019 October 23

ABSTRACT

We use a combination of data from the MaNGA survey and MaNGA-like observations in IllustrisTNG100 to determine the prevalence of misalignment between the rotational axes of stars and gas. This census paper outlines the typical characteristics of misaligned galaxies in both observations and simulations to determine their fundamental relationship with morphology and angular momentum. We present a sample of ∼4500 galaxies from MaNGA with kinematic classifications which we use to demonstrate that the prevalence of misalignment is strongly dependent on morphology. The misaligned fraction sharply increases going to earlier morphologies (28 ± 3 per cent of 301 early-type galaxies, 10 ± 1 per cent of 677 lenticulars, and 5.4 ± 0.6 per cent of 1634 pure late-type galaxies). For early-types, aligned galaxies are less massive than the misaligned sample whereas this trend reverses for lenticulars and pure late-types. We also find that decoupling depends on group membership for early-types with centrals more likely to be decoupled than satellites. We demonstrate that misaligned galaxies have similar stellar angular momentum to galaxies without gas rotation, much lower than aligned galaxies. Misaligned galaxies also have a lower gas mass than the aligned, indicative that gas loss is a crucial step in decoupling star–gas rotation. Through comparison to a mock MaNGA sample, we find that the strong trends with morphology and angular momentum hold true in IllustrisTNG100. We demonstrate that the lowered angular momentum is, however, not a transient property and that the likelihood of star–gas misalignment at $z = 0$ is correlated with the spin of the dark matter halo going back to $z = 1$.

Key words: galaxies: evolution – galaxies: haloes – galaxies: kinematics and dynamics.

1 INTRODUCTION

Angular momentum is one of the key properties that quantifies a galaxy. Within the Λ cold dark matter (ΛCDM) paradigm, galaxies form from the cooling and condensation of the initial gas cloud within dark matter haloes (Fall & Efstathiou 1980; Mo, Mao & White 1998). In this framework, the angular momentum content of the collapsing baryons are inherited from that of the surrounding dark matter halo (tidal torque theory (TTT); e.g. Hoyle 1951; Peebles 1969; Doroshkevich 1970). This is a natural result of the baryons and dark matter being well mixed at early times leading them to experience similar torquing from the surrounding tidal field of protohaloes.

If gravitational collapse proceeds unhindered, the initial gas cloud will form a stable rotating disc which eventually evolves into the late-type galaxies (LTGs) we observe today (White & Rees 1978). Since stars form from the rotating gas, the natural expectation is that they will inherit its dynamical characteristics leading to coherent rotation between dark matter, gas, and stars.

The evolution of a galaxy from initial collapse to today is, however, seldom completed in isolation. By its very nature, structure formation in ΛCDM is hierarchical with haloes undergoing bottom-up assembly from mergers of lower mass progenitors. After turnaround, the angular momentum of the baryons in a galaxy can be driven dramatically away from the expectations of TTT through external processes such as interactions or mergers. How such interactions alter angular momentum depend on the magnitude, orientation, and gas content of the merger. For example, gas-rich mergers in general spin-up galaxies whereas gas-poor mergers are seen to spin-down galaxies (Lagos et al. 2017, 2018).

Developments in spectrographs have led to the advent of integral field spectroscopy (IFS) which provides spatially resolved

★ E-mail: cd201@st-andrews.ac.uk

spectra for galaxies. Establishing work in the field has been the Spectrographic Areal Unit for Research on Optical Nebulae (SAURON; Bacon et al. 2001) and ATLAS^{3D} (Cappellari et al. 2011) surveys, which have focused on early-type galaxies (ETGs) in the local Universe. IFS has enabled kinematic classification through a proxy for angular momentum based on the stellar kinematics up to one effective radius (R_e). Termed λ_{Re}, the measure enabled the clear distinction between slow and fast rotating ETGs (Emsellem et al. 2007, 2011). While there is still debate over whether $1R_e$ is large enough to fully encapsulate the complete kinematic morphology of a galaxy (Foster et al. 2013; Arnold et al. 2014), it has opened the door for understanding the relationship between optical morphology and angular momentum.

IFS surveys for ∼1000 of galaxies across all optical morphologies are now a reality. For example, the Sydney-AAO Multi-object Integral field spectrograph survey (Croom et al. 2012; Bryant et al. 2015) has mapped ∼3400 galaxies upto $z \sim 0.12$ across a variety of environments. Even larger is the Mapping Nearby Galaxies at Apache Point (MaNGA; Bundy et al. 2015; Blanton et al. 2017) survey which will map ∼10 000 galaxies in the local Universe ($z = 0-0.15$). By design MaNGA will create a sample of near flat number density distribution across absolute *i*-band magnitude and stellar mass.

Recent studies in these surveys and also simulations have demonstrated the close interlink between stellar angular momentum, stellar mass, and morphology suggesting that late-types and early-type fast rotators form a continuous sequence rather than from fundamentally different formation pathways (Cortese et al. 2016; Lagos et al. 2017; Graham et al. 2018). Remarkably, despite the highly non-linear processes involved, current cosmological surveys predict that the stellar angular momentum in rotationally supported galaxies at $z = 0$ is still conserved from that of the dark matter halo (e.g. Genel et al. 2015).

In the extended theory of TTT, the spin of galaxies embedded in the larger scale environment of the cosmic web can be seen to align with the direction of filaments (e.g. Pichon et al. 2011; Codis, Pichon & Pogosyan 2015; Laigle et al. 2015). Low mass discs can accrete material most efficiently when its spin vector is aligned with the direction along the filament. Conversely, higher mass haloes can be formed through mergers in the plane along the filament, leading to a perpendicular spin alignment with the large-scale structure.

In this framework, it is then perhaps surprising to identify galaxies with decoupled rotation between the stars and gas. The ability of a given galaxy to accrete cold gas determines its continued ability to form stars and hence dictate where it falls amongst the Hubble sequence. Accreted gas, however, has many origins (such as filamentary 'cold mode' accretion from the cosmic web, mergers, or additionally cooling flows from a shocked hot halo) however is converted into stars within typical depletion time-scales of order gigayears (Davis & Bureau 2016). For material stripped in mergers or for shocked gas accreting through cooling flows, a natural consideration is that the accretion may not be necessarily aligned with the angular momentum of the benefiting galaxy (e.g. Davis et al. 2011; Lagos et al. 2015). Misalignment can be considered to be a transient property as torques from the stellar component continually act to realign the gas component which can only be opposed by sustained misaligned accretion (van de Voort et al. 2015; Davis & Bureau 2016).

Understanding the origin and nature of galaxies with decoupled star–gas rotation (kinematic misalignment – used interchangeably) has been the focus for several recent works. Davis et al. (2011) found that ∼36 per cent of ETGs exhibit misalignment between their star and gas rotation (i.e. difference of 30° between rotational axes) whose fraction increases for field ETGs. For late types, Chen et al. (2016) first investigated star forming galaxies with counter-rotating stars and gas, a far rarer occurrence (∼2 per cent), finding a clear boost in star formation in central regions. This suggests that the processes leading to misalignment are also inherent in cancelling angular momentum, enabling increased gas in-flows to nuclear regions. Jin et al. (2016) extended this discussion to find that for a sample of 66 misaligned galaxies, the misalignment fraction (>30°) is dependent on properties such as specific star formation rate, stellar mass, and local environment, again determining that misaligned galaxies are more isolated. Li et al. (2019) find that up-to 40 per cent of misaligned galaxies in MaNGA can be attributed to ongoing or recent mergers/interactions, underlining the importance of external processes (see also Barrera-Ballesteros et al. 2015). Duckworth et al. (2019b) explored the connection of misalignment in central galaxies to large-scale environment (i.e. distance to cosmic web) and halo assembly time, finding that 'cold' mode accretion from filaments was unlikely to contribute significantly to misalignment, noting that morphology held a far stronger relationship. Bryant et al. (2019) considered misalignments for ∼1200 galaxies in the SAMI survey also demonstrating that, rather than local environment, that morphology held the strongest correlation with likelihood of star–gas decoupling. Khim et al. (2019) compared this SAMI sample to the cosmological hydrodynamical simulation of Horizon-AGN, finding that current generation simulations do a surprisingly good job at reproducing overall misalignment fractions as a function of morphology. Starkenburg et al. (2019) considered the nature of counter-rotation (>90° between rotational axes of stars and gas) in low mass galaxies in Illustris. They identify the key role of gas loss through black hole (BH) feedback and flyby interactions to enable misalignment through re-accretion of misaligned material. The mechanisms for decoupling gas are not fully determined and are likely a combination of both external and internal processes, both of which are seen to also shape the stellar angular momentum content of galaxies at $z = 0$. To understand how these non-linear processes relate both to angular momentum retention from the dark matter halo and how this propagates to star–gas decoupling, a combination of both observations and simulations are required.

This article is the first in a series which will comprehensively categorize the nature of galaxies that have decoupled rotation between their stars and gas. Utilizing a combination of both state of art IFS observations (MaNGA) and simulations (IllustrisTNG100) the aim of the project is to demonstrate the fundamental relationships behind this decoupling. Here we introduce our observational sample[1] and mock sample in IllustrisTNG100. In this work we conduct a census of star–gas decoupling in both observations and simulations to study its link to galaxy morphology, stellar angular momentum, and spin of its parent dark matter halo. In the second paper in the series (Duckworth et al. 2019a), we use our simulated sample to better understand the relationship between black hole activity, misalignment, and gas properties. In future companion papers we will explore the causality of misalignment.

This paper is structured as follows. Section 2 describes the observational data we use in this work and our kinematic classifications.

[1]Full catalogue of kinematic classifications will be made publically available after the final MaNGA data release (2021). Classifications for currently public MaNGA data can be made available on request. See www.chrisduckworth.com for catalogue and Section 2 for description.

Section 3 describes the simulation data and our construction of the mock sample. Section 4 (Section 5) describes our results in MaNGA (IllustrisTNG100). Finally we discuss our findings in Section 6, before concluding in Section 7.

2 OBSERVATIONAL DATA

2.1 The MaNGA survey

Set to complete in 2020, the MaNGA survey is designed to investigate the internal structure of ∼10 000 galaxies in the nearby Universe. By design, the complete sample is unbiased towards morphology, inclination, and colour and provides a near flat distribution in stellar mass.

MaNGA is one of three programs in the fourth generation of the Sloan Digital Sky Survey (SDSS-IV) which enables detailed kinematics through integral field unit (IFU) spectroscopy. MaNGA uses the SDSS 2.5 metre telescope in spectroscopic mode (Gunn et al. 2006) with the two dual-channel BOSS spectrographs (Smee et al. 2013) and the MaNGA IFUs (Drory et al. 2015). MaNGA provides spatial resolution on kpc scales (2" diameter fibres) while covering 3600–10 300 Å in wavelength with a resolving power that varies from $R \sim 1400$ at 4000 Å to $R \sim 2600$ at 9000 Å.

MaNGA observations use SDSS style plates, where bundles of optical fibres are plugged into the plate corresponding to the position of the target galaxy in the observational field. A dithered pattern is employed for each target field (plate), which simultaneously observes galaxies through 17 fibre-bundles of five distinct sizes. Any incomplete data release of MaNGA should therefore be unbiased with respect to IFU sizes and hence a reasonable representation of the final sample scheduled to be complete in 2020. The majority of observations contribute to one of the three main subsets: the Primary sample, the Secondary sample, and the colour-enhanced supplement. All subsamples observe galaxies to a minimum of ∼1.5 effective radii (R_e) with the Secondary sample increasing this minimum to ∼2.5 R_e. The colour-enhanced supplement fills in gaps of the colour−magnitude diagram leading to an approximately flat distribution of stellar mass. A full description of the MaNGA observing strategy is given in Law et al. (2015), Yan et al. (2016b). The raw observations are processed by the MaNGA Data Reduction Pipeline (DRP) as described in Law et al. (2016), Yan et al. (2016a). The fibre flux and inverse variance is extracted from each exposure, which are then wavelength calibrated, flat-fielded, and sky subtracted. In this work, we use 6044 galaxies from the eighth MaNGA Product Launch (MPL-8) that are selected in the Primary, Secondary, and Colour-Enhanced samples and have non-critical observations. Fig. 1 shows the distribution of stellar mass and redshift of MPL-8 with comparison of our ΔPA defined sample (clear and coherent rotation in both stellar and Hα velocity fields) and those with coherent stellar rotation but no clear Hα rotation (NGRs). The latter two samples are fully described in Section 2.4.

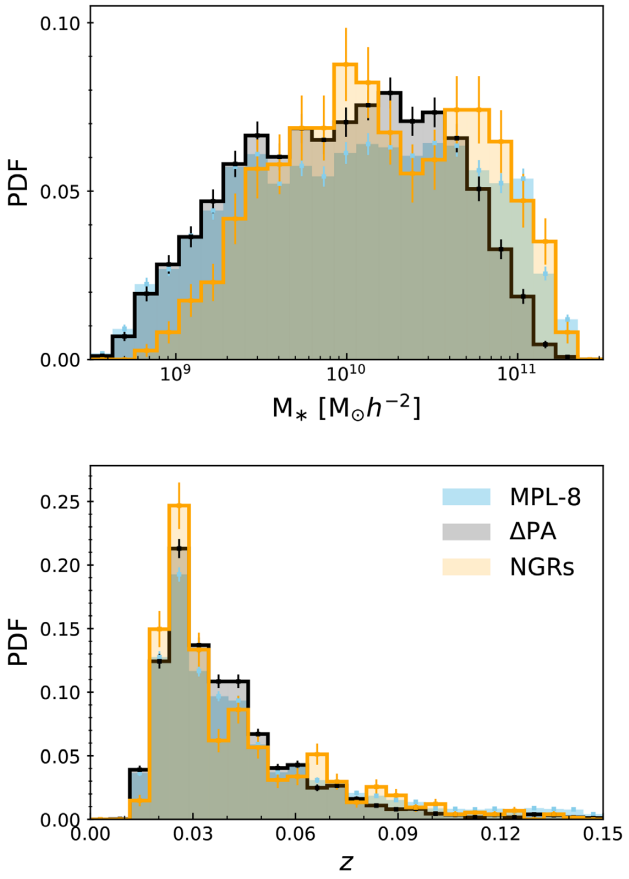

Figure 1. Relative frequency distributions of stellar mass (M_*) and redshift (z) for the MaNGA MPL-8 sample (light blue), our ΔPA defined sample (black), and those with a defined stellar PA but no clear Hα rotation (orange). The figure is cut at $z = 0.15$ representing the extent of MaNGA targets. Each histogram is given with Poisson errors on each bin.

2.2 Spectral fitting for kinematics

All stellar and Hα velocity fields are taken directly from the MaNGA Data Analysis Pipeline (DAP; Belfiore et al. 2019; Westfall et al. 2019, for an overview and emission line modelling, respectively), we direct the reader to these references, however we summarize the key points here.

The DAP extracts stellar kinematics using the Penalized Pixel-Fitting (pPXF) method (Cappellari & Emsellem 2004; Cappellari 2017). The DAP fits the stellar continuum of each spaxel to extract the line-of-sight velocity dispersion and then fits the absorption-line spectra from a set of 49 clusters of stellar spectra from the MILES stellar library (Sánchez-Blázquez et al. 2006; Falcón-Barroso et al. 2011). Before extraction of the mean stellar velocity, the spectra are spatially Voronoi binned to g-band $S/N \sim 10$, excluding any individual spectrum with a g-band $S/N < 1$ (Cappellari & Copin 2003). This approach is geared towards stellar kinematics as the spatial binning is applied to the continuum S/N, however, we note that unbinned and Voronoi binned velocity maps produce similar results.

Ionized gas kinematics are extracted by the DAP through fitting a Gaussian to the Hα-6564 emission line, relative to the input redshift for the galaxy. This velocity is representative for all ionized gas, since the parameters for each Gaussian fit to each emission line are tied during the fitting process. These velocities are also binned spatially by the Voronoi bins of the stellar continuum.

2.3 Defining global position angles

For a complete description of PA fitting and typical error estimation for MaNGA, we direct the reader to Duckworth et al. (2019b). Here we use a similar process, summarizing the key points and highlighting differences.

Global position angles (PA) are estimated for both the stellar and ionized gas velocity fields using the `fit_kinematic_pa` routine (see Appendix C of Krajnović et al. 2006, for a description of the process). `fit_kinematic_pa` returns the angle (counter-clockwise) of the bisecting line which has greatest velocity change along it. The best-fitting angle is found by sampling 181 equally spaced steps, so that the output PA will have precision of 0.5°. By default, `fit_kinematic_pa` returns a PA defined between 0° and 180°, which is indiscriminate towards direction of the blueshifted and redshifted sides. To adjust this, we identify the redshifted side and return PAs defined by the angle to the redshifted side clockwise from the north axis (0–360°).

The accuracy of PA fitting is biased by neighbouring galaxies, spectral pixels (spaxels) with spuriously high velocities and inclination. Foreground stars are removed during the spectral fitting, however foreground/background galaxies can remain within the IFU footprint. This can be a significant problem for global PA fitting since `fit_kinematic_pa` naturally interprets other material as part of the target galaxy's observation and interpolates between the regions. Background/small objects can then bias the PA fit for the main target, especially in the instance where they are moving significantly different to the target galaxy (e.g. when they are at different z). To counteract this, we remove all disconnected regions smaller than 10 per cent of the target galaxy's footprint. To ensure a PA fit robust to small-scale fluctuations in the velocity field, `fit_kinematic_pa` symmetrizes (averages the magnitude) across each quadrant of the velocity field. However, spaxels with spuriously high velocities (e.g. $>1000\,\mathrm{km\,s^{-1}}$ relative to target's central redshift) can still bias PA fits during symmetrization, if the region is large enough. These often correspond to background galaxies that are connected (on the sky) to the target galaxy's footprint, and hence, we sigma clip the velocity field and remove all spaxels above a 3σ threshold.

Accurate PA estimation is naturally more difficult for near perfect edge-on galaxies. Disc obscuration and a smaller surface area allow individual Voronoi bins to more easily bias overall PA fits. This inherently leads to a larger scatter in PA fitting around the true value, especially due to central spaxels during symmetrization. Detecting misalignment (equation 1) in near perfect edge-on galaxies is also difficult due to projection effects. For these reasons, we remove all galaxies close to pure edge-on where we would be unable to distinguish between aligned and misaligned (as described in Section 2.5).

2.4 Visual classifications

Global position angles are only well defined for coherently rotating velocity fields. Those with a decoupling between inner and outer regions due to warps or kinematically decoupled cores (KDCs) are poorly described by global PAs. To select a clean sample of galaxies with well-defined global PAs, we visually classify all of the velocity fields after pre-processing and PA fitting. Both stellar and Hα velocity fields are characterized into three categories:

(i) Dominant coherent rotation and well-defined PA.
(ii) Dominant coherent rotation but with more noise or more complex motion resulting in a usable PA fit but with higher typical errors. Highly inclined velocity fields with a higher likelihood of inaccurate PAs fits are included in this category.
(iii) Do not use.

Kinematic features are also identified. Both stellar and Hα velocity fields are classified into:

(i) Kinematically decoupled core (i.e. those with a central component that rotates in a different direction (>30°) with respect to the overall galaxy rotation).
(ii) Warp (velocity field of central region is warped with respect to outskirts. This may be due to a bar, oval shaped structures in the disc (oval distortions), or accretion of fresh material with different angular momentum to the bulk rotation).
(iii) Merger (ongoing merger or neighbour identified within IFU. Only those with obvious disruption are followed up in photometry).
(iv) No features.

The majority of those with kinematic features have poorly defined global PAs and hence are flagged as do not use for the previous flag. The galaxies we refer to as 'warped' represents a combination of galaxies with bars, oval distortions, and differential rotation in the disc (e.g. Barrera-Ballesteros et al. 2014). We direct the reader to Stark et al. (2018) for an approach to separate the galaxies we refer to as warps. In this work, we enforce axisymmetry for our sample and hence make no use of galaxies that have significant variations in their PA as a function of radius.

For studies of quenching it may be useful to consider galaxies that have defined stellar rotation but lack coherent motion in the ionized gas. For galaxies that have usable PAs for the stellar velocity but unusable PAs for the ionized gas, we define a further classification of the gas velocity field:

(i) Depletion (seen as empty spaxels signifying lack of gas, usually in central regions)
(ii) No clear rotation (map has no clear rotation or is noise dominated)
(iii) Partial rotation (partial coherent rotation in the velocity field, however there are significant regions with incoherent motion or noise domination)
(iv) No clear characteristics/ no gas.

We note that there is a clear overlap between the classifications for depletion and no clear rotation, since velocity fields are often a combination of these two features. The total numbers for each classification in each category are summarized in Table 1. Examples of PA fits (see Section 2.5 for calculation) with the associated photometry for various kinematic classifications is given in Fig. 2. Examples of galaxies that are kinematically aligned, misaligned, have a stellar kinematically decoupled core, have a warped Hα velocity field and have clear stellar rotation but depleted ionized gas/no rotation are shown, respectively.

2.5 Defining kinematic misalignment

Only selecting galaxies with dominant coherent rotation (both clean and messy) for both stellar and Hα velocity fields with no defined features in either map, we are left with 3798 galaxies that make up our ΔPA defined sample used in this analysis. The mass distribution of the ΔPA defined sample with respect to MPL-8 is shown in Fig. 1. We define the offset angle between the kinematic PAs of the stellar and ionized gas fields as such:

$$\Delta\mathrm{PA} = |\mathrm{PA}_{\mathrm{stellar}} - \mathrm{PA}_{\mathrm{H}\alpha}|. \quad (1)$$

We define galaxies with $\Delta\mathrm{PA} \geq 30°$ to be significantly kinematically misaligned. Galaxies with $\Delta\mathrm{PA} < 30°$ are referred to as aligned. The choice of ΔPA is somewhat arbitrary, however, is chosen

Table 1. Summary table of galaxy numbers for kinematic classifications in MPL-8. Each row shows the total number of galaxies in the classification criteria defined in each column for stellar velocity fields only, gas velocity fields only and both (top to bottom). Columns 1–3 correspond to the quality of the PA fit, 4–6 correspond to kinematic features, and 7–9 correspond to additional notes for the Hα velocity field (see the text for details about classifications). Columns 7–9 are only defined for unusable PAs for Hα and clean/messy PAs for the stellar field. The total number of galaxies meeting this criteria is given in the stellar row for columns 7–9.

	Clean PA	Messy PA	Unusable PA	KDC	Warp	Merger	Depletion	No clear rotation	Partial rotation
Stellar	3290	1581	1172	47	39	116	960	960	960
Hα	2876	1071	2097	17	82	116	562	180	175
Both	2848	1023	1136	5	11	116	–	–	–

for comparison with previous literature (e.g. Davis et al. 2011; Bryant et al. 2019). Regardless 30° represents a conservative choice for selecting galaxies with significant decoupling; the reasons for which are twofold. First, since we are comparing the ionized gas in MaNGA to all gas in IllustrisTNG100, we must take into account the different kinematic properties of different gas phases. In observation, Davis et al. (2013) find that the typical difference between the PAs of cold gas (CO) and ionized gas can be described by a Gaussian distribution centred on 0 with a standard deviation of 15° for 38 CO bright galaxies in ATLAS^{3D}. While indicating ionized gas is a reasonable estimator for cold gas, splitting at ΔPA = 30° accounts for the scatter in this relationship. Secondly the split takes into account both the error in ΔPA estimation (a few °; see Appendix A3 of Duckworth et al. 2019b) and projection effects since it is a projection of a 3D property. We note that taking a different split at 40° does not change any of our findings.

2.6 Morphology

We classify the morphology of MaNGA galaxies through the formalism laid out by the citizen science project; GalaxyZoo2 (GZ2; Willett et al. 2013). GZ2 provides visually identified morphologies (and also measures finer morphological features, e.g. bars, bulge size, and edge-on discs) for 304 122 galaxies drawn from SDSS. GZ2, however, is not complete for the MaNGA sample and has been combined with an unpublished version; GalaxyZoo4 to provide a consistent set of definitions for all MaNGA targets (see https://www.sdss.org/dr15/data_access/value-added-catalogs/?vac_id = manga-morphologies-from-galaxy-zoo).

In a nutshell, GZ2 provides morphological classification through a decision tree of questions. Further questions are dependent on the answer to the previous to characterize a certain morphological type and identify finer features (see fig. 1 in Willett et al. (2013) for this flowchart). From this, a table of vote fractions for each question combined with the total number of votes dictate a reliably sampled galaxy population with a set of desired morphological features. Votes by individuals are debiased (weighted) based on their reliability in comparison to known answers to the questions.

The first question in the decision tree 'Is the galaxy smooth and rounded with no sign of a disc?', allows categorization into broad ETGs and LTGs. We select galaxies with a debiased vote fraction >0.7 for smooth to be ETGs and galaxies with a debiased vote fraction of >0.7 for disc or features to be LTGs. Defining an exact population of lenticular galaxies (S0s) is tricky through public classifications. LTGs, however, can be separated based on the dominance of the bulge with respect to the disc in GZ2 through the question 'How prominent is the central bulge, compared with the rest of the galaxy?'. Willett et al. (2013) demonstrate a strong correlation between bulge dominance as defined per this question and expert classifications of T-type (Nair & Abraham 2010). Equation (19) of Willett et al. (2013) provides a linear mapping from GZ2 bulge classification to expert defined morphological T-type. Care must be taken in using this linear mapping (see discussion in Willett et al. 2013), however, this should be a reasonable parametrization to coarsly separate LTGs into earlier-type (S0 - Sa) and later-type spirals (Sb - Sd). We split our LTG population at T-type = 3, to give two morphological categories; S0-Sas and Sb-Sds in addition to pure ETGs.

The estimates of gas mass used here for MaNGA are derived from the Pipe3D pipeline (Sánchez et al. 2016, 2018), which uses dust attenuation within the footprint of the IFU, which methodology is described in Barrera-Ballesteros et al. (2018).

2.7 Group membership

To investigate different pathways leading to kinematic misalignment, we must separate galaxies into centrals and satellites. We identify groups with an adaptive halo-based group finder of Yang et al. (2005), Yang et al. (2007) and with improved halo mass assigning techniques (see Lim et al. 2017, for details and application to SDSS). In a nutshell, the group finder uses either the stellar mass or luminosity of central galaxies in addition with the nth brightest/most massive satellite as proxies for halo mass. Galaxies are assigned to groups through an iterative process, where halo properties such as halo size and velocity dispersion are updated until membership converges.

Lim et al. (2017) do not apply the group finder to the thin strips in the Southern Galactic Cap of SDSS mainly due to incomplete groups resulting from close proximity to borders. MaNGA galaxies in these strips are therefore unclassified by the group finder, resulting in 5088 matched galaxies with group membership classifications into central or satellite.

3 SIMULATION DATA

3.1 IllustrisTNG

The IllustrisTNG project (Marinacci et al. 2018; Naiman et al. 2018; Nelson et al. 2018; Springel et al. 2018; Pillepich et al. 2018b) is a suite of magnetohydrodynamic cosmological scale simulations incorporating an updated comprehensive model for galaxy formation physics (as described in Weinberger et al. 2017; Pillepich et al. 2018a) and making use of the moving-mesh code AREPO (Springel 2010; Pakmor, Bauer & Springel 2011; Pakmor & Springel 2013). For this work, we use the highest resolution fiducial run of TNG100 which follows the evolution of 2×1820^3 resolution elements within a periodic cube with box lengths of 110.7 Mpc (75 h^{-1} Mpc). This corresponds to an average mass resolution of

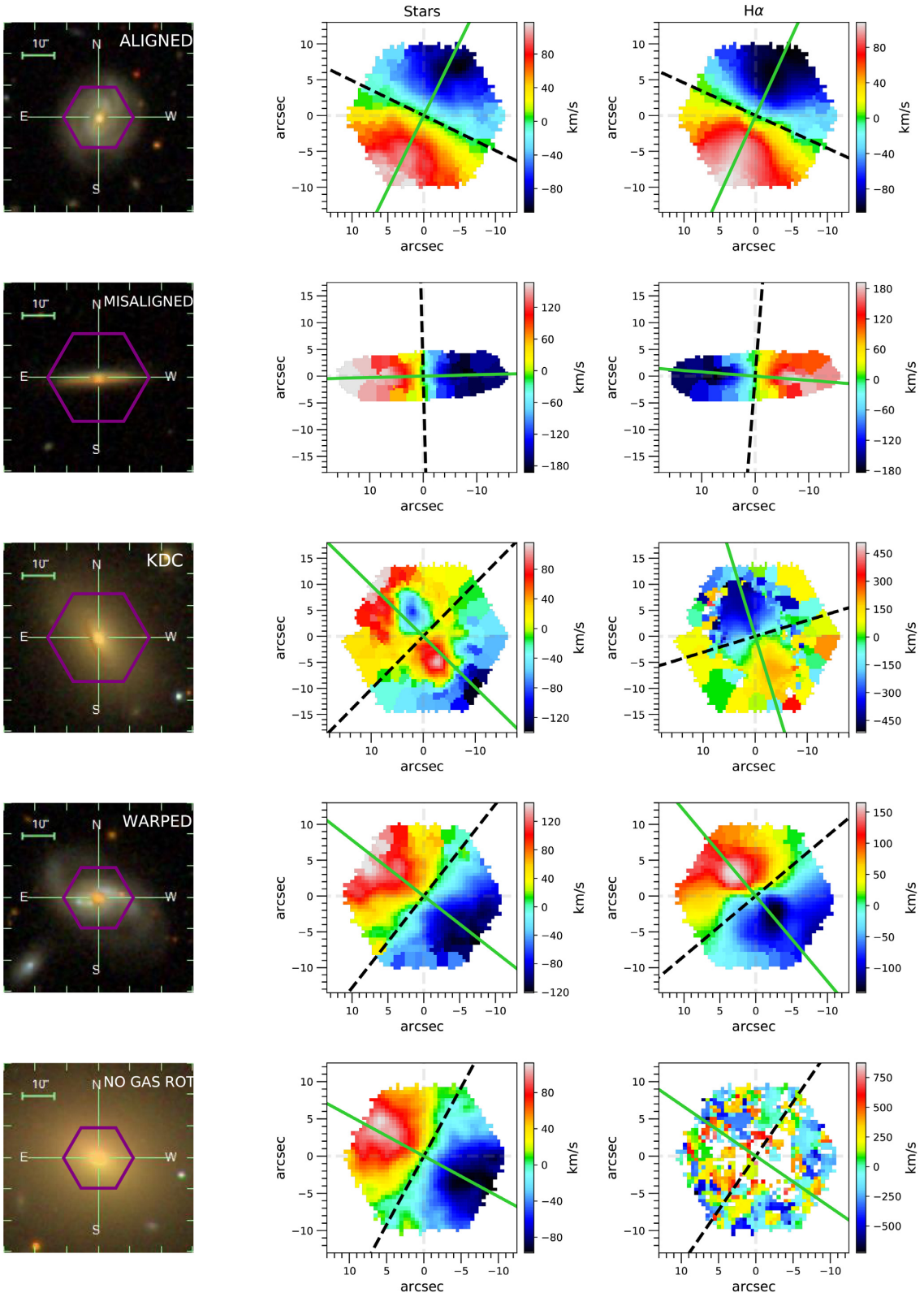

Figure 2. Examples of PA fits for galaxies with different kinematic classifications. For each galaxy (row), we show the photometry taken from SDSS with the MaNGA IFU observation footprint overlaid in purple (left-hand panel), the stellar velocity field (middle), and the Hα velocity field (right-hand panel). The kinematic PA fits (see Section 2.5) are shown on the velocity fields (green solid line) with the axis of rotation (black dotted line). The kinematic classifications from top to bottom are (a) PLATEIFU: 7958-6101, kinematically aligned near face on; (b) PLATEIFU: 8465-12704, counter-rotating near edge on; (c) PLATEIFU: 9868-12704, with a KDC in the stellar velocity; (d) PLATEIFU: 8252-6103, with a warped Hα velocity field with respect to the stellar; (e) PLATEIFU: 10219-6102, with a centrally depleted/missing Hα velocity field but coherent rotation in the stellar.

baryonic elements of $1.4 \times 10^6\,M_\odot$ and $7.5 \times 10^6\,M_\odot$ for dark matter. Here we make use of public data from the IllustrisTNG project (as described in Nelson et al. 2019).

Structure in TNG100 is identified into haloes and subhaloes as follows. Haloes (also referred to as FoF haloes or Groups) are found from a standard friends-of-friends (FoF) algorithm (Davis et al. 1985) with linking length $b = 0.2$. The FoF algorithm is run on the dark matter particles, and the other types (gas, stars, BHs) are attached to the same groups as their nearest DM particle. Each halo is then divided into gravitationally bound subhaloes through the subfind algorithm (Springel et al. 2001). In short, subfind defines 'subhaloes' as locally overdense and self-bound particle groups as distinct objects within given FoF haloes. We consider all subhaloes at $z = 0$ containing a minimum stellar mass of $M_* = 10^{8.5}\,M_\odot$ to potentially make up our mock MaNGA like sample. Since we are typically considering the stellar component of these subhaloes for our mock observations, we will refer to these as TNG100 galaxies.

3.2 Matching to MaNGA sample

To construct a mock MaNGA sample we select representative subhaloes from TNG100. For every MaNGA galaxy, we find the TNG100 galaxy with the most similar stellar mass, size, and SDSS $g - r$ colour. In this instance, stellar mass is defined by the total mass of stellar particles within a radius of 2 stellar effective radii. The SDSS $g - r$ colour is found using the prescription outlined in Nelson et al. (2018). Here we describe the general process, while we direct the reader to Nelson et al. (2018) for more detail. Each stellar particle in the simulation is modelled as a single-burst simple stellar population. This is converted into a population spectrum using FSPS (Conroy, Gunn & White 2009; Conroy & Gunn 2010; Foreman-Mackey, Sick & Johnson 2014) which is convolved with the pass-bands for SDSS colours. We use model C (as described in Nelson et al. 2018) which also includes models for unresolved and resolved dust. We use sizes following the prescription of Genel et al. (2018), which use a projected half-light radius. The SDSS bands are constructed as above and are used to define circular half-light radii for each SDSS band along X, Y, and Z projections of the box. We use the *r*-band half-light radius projected perpendicular to the XY plane, consistent with the line of sight of the mock MaNGA observation.

The matching is done through finding the closest neighbour in a normalized space with dimensions of the matched properties. If multiple MaNGA objects match to a given TNG100 galaxy then the absolute nearest neighbour is selected and the MaNGA object is assigned to its second nearest neighbour. The process is iterated until all have unique matches.

The galaxy is then assigned the same bundle size IFU as the matched MaNGA galaxy with the corresponding angular resolution. The galaxy is then 'observed' (see Section 3.3) at a distance so that the angular footprint of the assigned IFU covers the same number of physical effective radii for the mock galaxy as the matched observation.

3.3 Mock observations

We convert each galaxy in TNG100 into a mock MaNGA observation, as follows:

We take the raw particle/cell data of gas and stars and project on the XY plane (i.e. z-direction is the line of sight). Since there is no preferred direction in the simulation, this corresponds to a 'random' viewing angle of each galaxy. We bin particles corresponding to the angular resolution of spaxels in MaNGA (0.5 arcsec pixel^{-1}), in the distinct hexagonal footprint of MaNGA observations. In each bin, we calculate the mean velocity, velocity dispersion, and total flux for all particles.

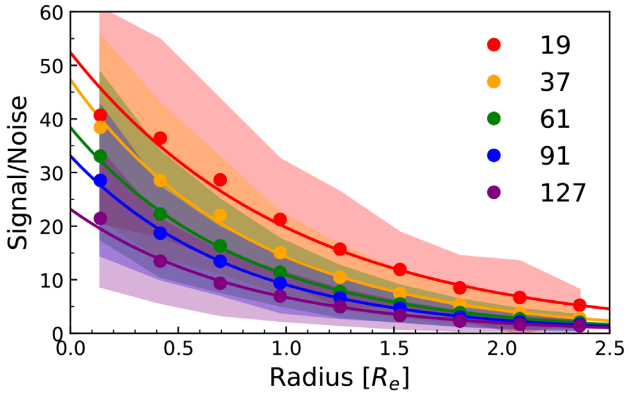

Figure 3. Average signal-to-noise profiles for each IFU size for all MaNGA MPL-8 observations. The circles show the median value for each radius bin with the shaded region corresponding to the standard deviation. The solid line corresponds to an logarithmic parametric fit to the data points, used in sampling the noise profile for the mock observations.

Since we include all particles along the line of sight, we must take care in interpreting the absolute values of flux, since none is lost due to obscuration. We, however, do not use the flux values calculated here in our work.

In order to estimate the typical noise associated with a MaNGA observation, we compute radial profiles of the signal-to-noise ratio (SNR) for all MaNGA observations of a given IFU size. MaNGA has five different IFU sizes corresponding to bundles of 19, 37, 61, 91, and 127 fibres. MaNGA provides estimates of the SNR for every spaxel in each observation in the *g*-band. Fig. 3 shows the azimuthally averaged SNR profiles for all MaNGA observations of each fibre bundle size. We fit a logarithmic function to each profile, which is used to assign noise to the mock observations. Noise is drawn for each pixel from a normal distribution using the median and standard deviation of the fitted logarithmic radial profile.

In order to simulate the effects of the point spread function (PSF), we then convolve our binned particle data with a Gaussian kernel. MaNGA observations typically have a *g*-band PSF which can be fit with a Gaussian of $\sim$2−3 arcsec full width half-maximum (FWHM). We take all our mock observations to have a PSF modelled by a Gaussian with a 2 arcsec FWHM.

We fit position angles to MaNGA observations that have been Voronoi binned so that bins contain a minimum S/N $\sim$10. To maintain consistency and avoid spurious individual particles biasing measurements, we also Voronoi bin our mock observations so that a minimum of five particles is contained within a given bin, again using the routine of Cappellari & Copin (2003). Fig. 4 shows example stellar (and gas) velocity and dispersion fields along with normalized *r*-band flux, after our processing.

4 MISALIGNED GALAXIES IN MANGA

4.1 Total population

First we consider all ΔPA defined galaxies for both MaNGA and TNG100. Fig. 5 shows the distribution of ΔPA for both MaNGA and IllustrisTNG100. Both distributions are strongly peaked around

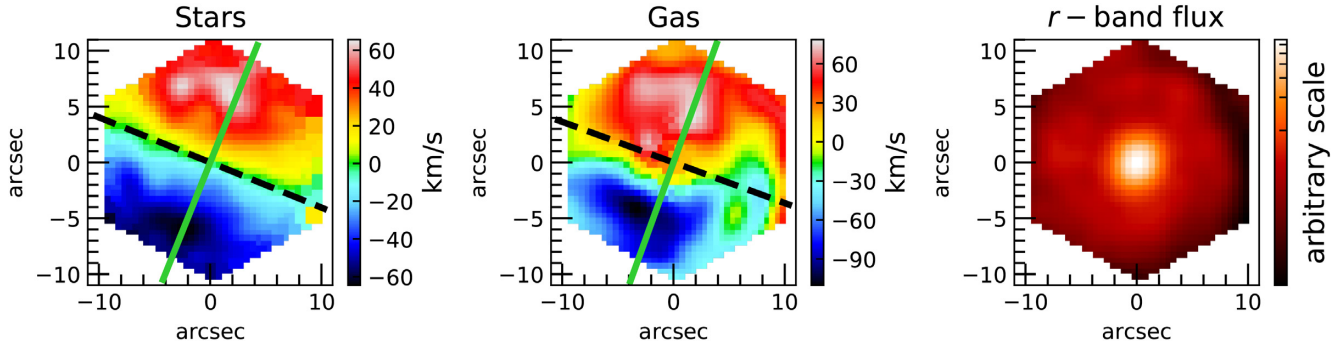

Figure 4. Example outputs from a MaNGA-like observation in TNG100. Shown (left to right) are the stellar velocity field, gas velocity field, and normalized *r*-band flux for a given galaxy, 'observed' under the same conditions of its MaNGA counterpart (i.e. distance and IFU size). For the stellar and gas velocity fields, the kinematic PA fits (see Section 2.5) are shown (green solid line) with the axis of rotation (black dotted line).

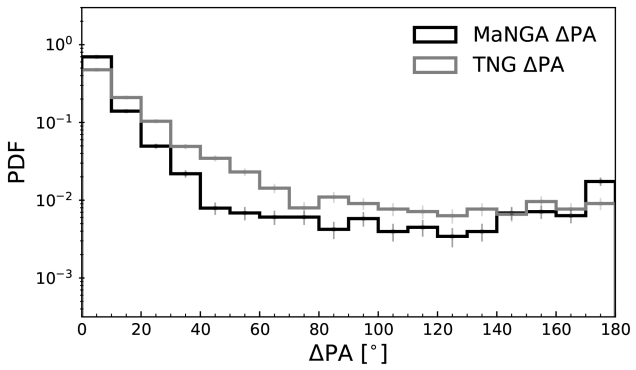

Figure 5. Probability density distribution of kinematic misalignment as defined by ΔPA for the total MaNGA sample (black line) and matched TNG100 sample (grey line). ΔPA is strongly peaked around 0° with a small boost close to 180°.

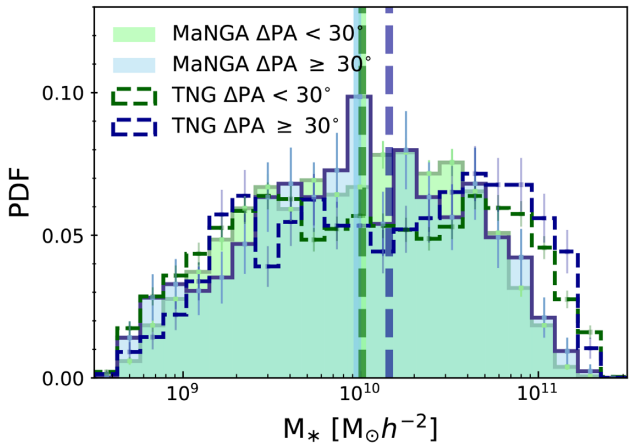

Figure 6. Probability density distributions of stellar mass, ($M_*/M_\odot$) for aligned galaxies (ΔPA < 30°, green) and misaligned galaxies (ΔPA > 30°, red) defined in MPL-8 (solid lines) and TNG100 (dashed). The vertical lines denote the corresponding distribution's median. The overall distributions are a reasonable match between mocks and observations, with a noted preference for ΔPA defined galaxies at the very high mass end for TNG100.

around 0° indicative of the preferentially aligned state predicted from tidal torquing theory. The MaNGA distribution shows a sharp drop-off past 40° whereas TNG100 shows a smoother drop off to higher misalignments. Additionally the MaNGA distribution shows a second peak around 180° indicative of the stable counter-rotating state identified in previous work (e.g. Chen et al. 2016). This secondary peak is not seen for the overall TNG100 sample, however is apparent for star forming galaxies in TNG100 (see bottom panel of Fig. 12).

The TNG100 mock sample reproduces the general trends well, when considering the differences in how we split the samples in observations and simulations. The smoother drop-off past 40° for TNG100 is likely a combination of how we construct the mock observations and scatter in the mass distributions between the MaNGA and TNG100 samples. By construction the matching between MaNGA and TNG100 objects is done before ΔPA is calculated. For this reason there may be differences between the mass distribution of the ΔPA defined MaNGA and TNG100 samples, as shown in Fig. 6. We find that the misaligned sample in TNG100 is slightly more massive with respect to MaNGA whereas the aligned samples are consistent. Due to the strong morphological dependence on kinematic misalignment, there is a secondary dependence on stellar mass. The increased overall fraction of misaligned galaxies in TNG100 is therefore, in part, due to the TNG100 ΔPA defined sample being slightly more massive. This slight boost could indicate that the mechanisms for misalignment may be different in simulations than observations. Khim et al. (2019) compare the misalignment fractions in observations (SAMI) with simulations (Horizon-AGN). While overall a good agreement is found, they note a significant difference in cluster environments where simulated galaxies are far more likely to be misaligned than in observations. More work needs to be done to understand how well cosmological hydrodynamical simulations replicate the processes leading to misalignment in observations, however, overall trends appear to be well reproduced for different simulation prescriptions.

For the rest of this section, we will only consider the properties of MaNGA galaxies leaving the results of the TNG100 mock sample to Section 5. We divide our MaNGA ΔPA defined population at ΔPA = 30° into aligned and misaligned. In the following, we also consider galaxies with defined stellar PAs but undefined Hα due to central depletion or incoherent rotation/dispersion domination (no gas rotation; NGRs). Fig. 7 shows the distribution of stellar mass for these three populations. We see no significant difference between

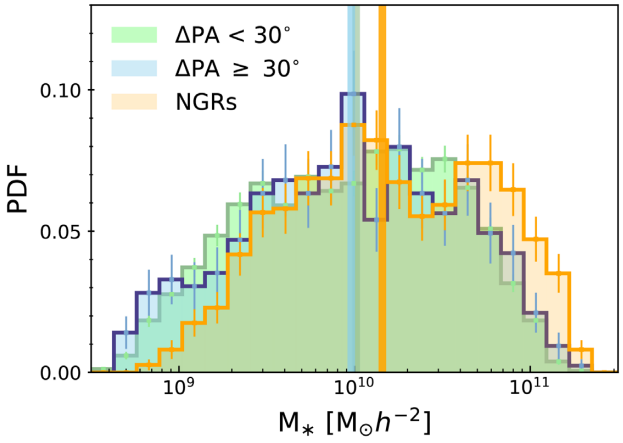

Figure 7. Probability density distributions of stellar mass, ($M_*/M_\odot$) for aligned galaxies ($\Delta PA < 30°$) shown in green, those with high misalignment ($\Delta PA > 30°$) are in blue and NGRs are in orange. Each histogram is given with Poisson errors on each bin. The vertical lines denote the corresponding distribution's median. NGRs are typically at higher stellar mass than those with aligned star and gas rotation.

the aligned and misaligned galaxies, however NGRs appear to be slightly more massive. Graham et al. (2018) previously demonstrated the tight correlation between stellar angular momentum and stellar mass for MaNGA (∼2300 galaxies). Since NGRs and misaligned galaxies are slightly higher mass, it could be expected that they are typically less rotationally supported with respect to the ΔPA defined populations.

Here we use the luminosity-weighted stellar angular momentum estimator, λ_R, taken directly from equation (1) in Emsellem et al. (2007) as

$$\lambda_R \equiv \frac{\langle R|V|\rangle}{\langle R\sqrt{V^2+\sigma^2}\rangle} = \frac{\Sigma_{n=1}^{N} F_n R_n |V_n|}{\sum_{n=1}^{N} F_n R_n \sqrt{V_n^2+\sigma_n^2}}. \quad (2)$$

λ_R is calculated from summing over N pixels in the IFU observation within the radius of interest, R. F_n, V_n, and σ_n are the flux, line-of-sight velocity, and line-of-sight velocity dispersion of the nth pixel. Here we present all measures of λ_R encompassing a radius of $1.5R_e$ weighted by r -band flux. We also take the ellipticity to be $\epsilon = 1-b/a$ where a and b are the major and minor axes of the galaxy estimated from the NASA Sloan Atlas catalogue (used for target selection in MaNGA; Blanton et al. 2011).

Fig. 8, shows λ_R versus ϵ for all ΔPA defined galaxies and the medians for the aligned, misaligned, and NGR samples. The black solid line overlaid shows the slow rotator regime (enclosed in bottom left). The fast/slow rotator classification refers to whether a given galaxy's rotation can be considered regular (circular velocity) or exhibits dispersion-dominated motion (Emsellem et al. 2007). Kinematically aligned galaxies reside at preferentially higher λ_R and ellipticity with respect to NGRs. This is indicative of the dispersion dominance over rotation for disrupted gas-poor and typically higher mass galaxies that we see in our NGR sample. Interestingly, kinematically misaligned galaxies also typically reside close to the slow rotator regime. In addition, the same qualitative trends are seen (i.e. misaligned and NGR galaxies have lowered angular momentum with respect to the aligned) are seen if this plot is made for ETGs, S0-Sas, or Sb-Sds alone.

In Fig. 9 we show the distribution of gas masses for the aligned, misaligned, and NGRs. We see a clear trend of lower gas mass going from kinematically aligned galaxies to misaligned galaxies to NGRs. We note that the majority (∼80 per cent) of NGRs do not contain enough gas to have a measured gas mass from the routine of Pipe3D, so the distribution shown is a hard upper limit on the gas that these galaxies contain. We note that these trends remain qualitatively the same when considering the distributions for ETGs, S0-Sas, and Sb-Sds individually.

The similarity in stellar angular momentum between the NGRs and kinematically misaligned galaxies could indicate that they are from the same evolutionary sequence. A key component in decoupling star–gas rotation in simulations is a significant gas loss followed later by the accretion of material with misaligned angular momentum (van de Voort et al. 2015; Starkenburg et al. 2019). This gas loss can happen due to interactions from neighbouring galaxies which strips gas or through ejection due to black hole feedback.

In Duckworth et al. (2019b), it was shown that kinematic decoupling shows little relationship with distance to filamentary structure. This could point to stripped/ejected material being re-accreted as a potential source of misalignment between star and gas rotation. Some NGRs could therefore represent an earlier timestamp before this material is re-accreted. Not all NGRs would necessarily re-accrete gas, meaning that some would remain quenched (and hence would not become misaligned in the future) potentially explaining the differences we see in stellar mass distributions of NGRs and misaligned. In this scenario, it would suggest that re-accretion of new material does not significantly alter the stellar angular momentum content going from NGRs to misaligned.

4.2 Morphology

We now sub-divide the total population by morphology into ETGs, S0-Sas, and Sb-Sds as defined in Section 2.6. Fig. 10 shows the distributions for each category. We find that for all morphological types, galaxies are most commonly aligned with strong peaks below ΔPA ∼30°. ETGs show a flatter distribution than their later counterparts, as the most likely to exhibit misalignment. LTGs show deeper drop-offs above ΔPA ∼40°, with a boost around ΔPA = 180°, seen most strongly for the Sb-Sds. We quantify the overall misalignment fractions in the first column of Table 2. Our errors are estimated by binomial counting errors so that $\sigma = \sqrt{p(1-p)/M}$ where $p = N/M$ with N being the number of misaligned galaxies and M the total number of galaxies for the category.

This morphological difference in misalignment is likely a result of several factors. Gas-rich LTGs have typically higher specific angular momentum, and hence, require a higher magnitude gas inflow/outflow with different angular momentum to disrupt rotation and create misalignment. Conversely, ETGs are more dispersion-dominated and gas-poor enabling smaller gas in-flows (or outflows) to create a kinematic misalignment.

These results are reasonably consistent with previous findings of 36 ± 5 per cent (of 260 galaxies) of ETGs that are misaligned in ATLAS^{3D} and in SAMI (45 ± 6 per cent of 36 pure ellipticals, 5 ± 1 per cent in 221 pure late spirals) (Davis et al. 2011; Bryant et al. 2019). We note that our ETG misalignment fraction (∼28 per cent) is lower than these previous findings and holds a slight tension with Bryant et al. (2019). Possible reasons for the differences may be due to morphology definition, stellar mass distribution, or simply sample size. We note that enforcing stricter thresholds for morphology classifications does not change our misaligned fractions pointing to a likely difference in mass distributions or our increased sample size.

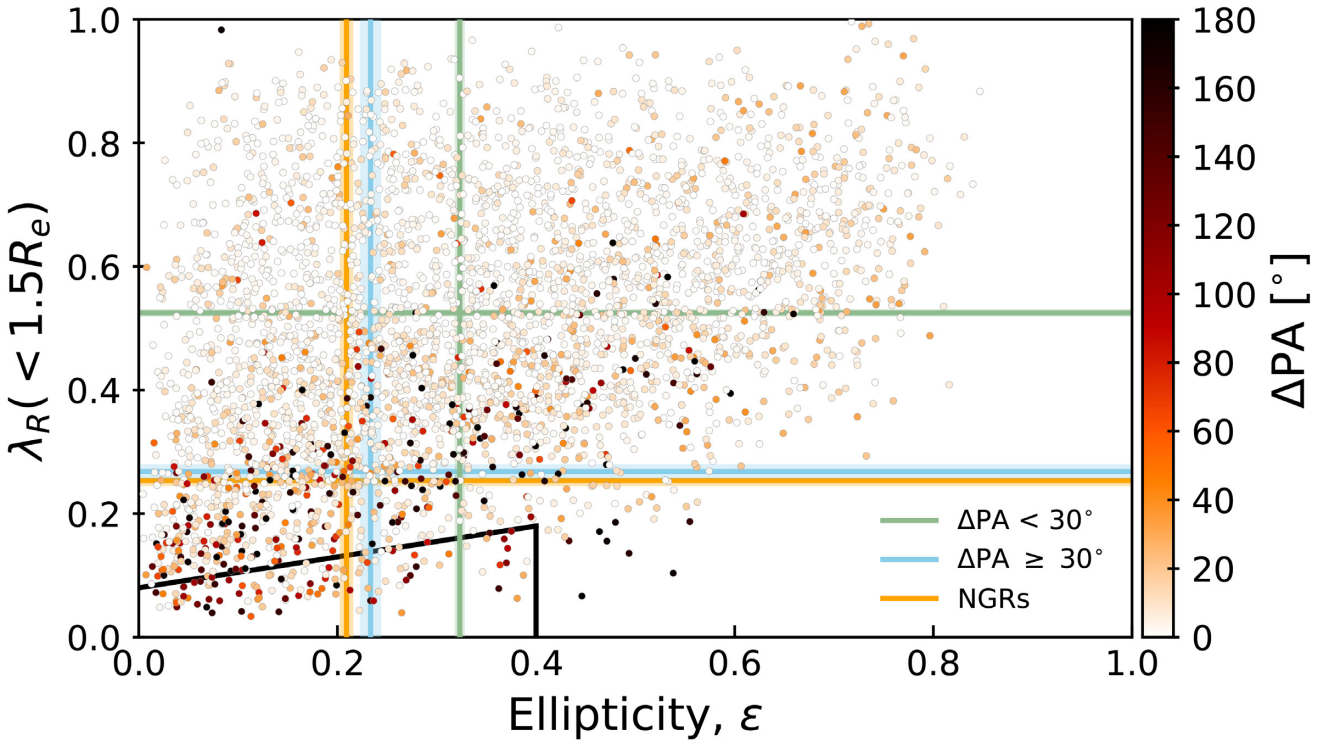

Figure 8. λ_R within $1.5R_e$ against ellipticity, ϵ for all galaxies with defined ΔPA. The individual points are for all ΔPA defined MaNGA galaxies coloured by ΔPA according to the colourbar. Medians for kinematically aligned (ΔPA < 30°), misaligned (ΔPA > 30°), and NGRs are shown by the green, light blue, and orange lines, respectively. The lighter shade around each line corresponds to the standard error. Aligned galaxies reside more typically in the fast rotator regime with higher λ_R and ϵ, whereas misaligned galaxies and NGRs reside closer to the slow rotator regime. The same qualitative trends are found if this plot is made for ETGs, S0-Sas, or Sb-Sds alone.

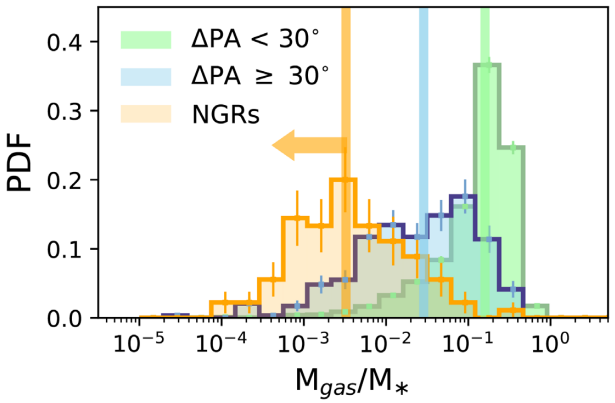

Figure 9. Probability density distributions of gas mass fraction, (M_{gas}/M_*) for aligned galaxies (ΔPA < 30°) shown in green, those with high misalignment (ΔPA > 30°) in light blue and NGRs in orange. Each histogram is given with Poisson errors on each bin. The vertical lines denote the corresponding distribution's median. The majority of NGRs do not have detectable gas masses and therefore the distribution shown should be considered as upper bound.

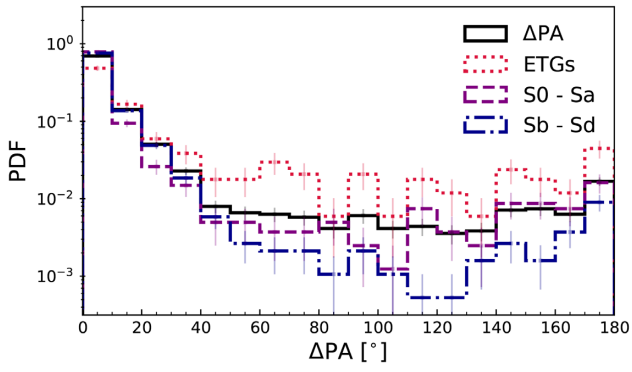

Figure 10. Probability density distributions of kinematic misalignment as defined by ΔPA split on morphology. The probability density distribution is normalized to 1 and shown in log scale. Distributions for the total population, ETGs, S0/Sa, and Sb-Sds are shown by black solid, dotted red, dashed purple, and dot-dashed blue lines, respectively. Earlier type galaxies are more likely to be misaligned than later type galaxies.

The boost in the PDF around 180° of Fig. 10 suggests that near counter-rotation is a stable state for galaxies. This is seen most prominently in Sb-Sds with a clear upwards trend in the PDF from ∼140°. A possible explanation is that these rotation-dominated galaxies host strong stellar torques, which act to realign gas at intermediate misalignments (30°<ΔPA <150°) on much faster time-scales than in ETGs. Counter-rotators, however, remain stable and hence contribute proportionally higher to the misaligned distribution, in comparison to those at intermediate misalignments which settle towards alignment or counter-rotation.

Interestingly galaxies that exhibit near-counter rotation (ΔPA ≥ 150°) have similar stellar angular momentum to the general misaligned population (ΔPA ≥ 30°), significantly lower than the

Table 2. Total number of galaxies used in this study for each of ΔPA defined sample, of those that are kinematically misaligned and those that have well defined stellar rotation but incoherent gas (NGR). These are defined for both splitting on morphology (rows) and group membership (columns). For those that are kinematically misaligned (ΔPA $\geq$30°), the percentage with respect to all those with ΔPA measurements for the sub-category is shown. The uncertainties quoted are binomial counting errors.

		All	Centrals	Satellites
All galaxies	ΔPA defined	3798	2185	1007
	ΔPA $\geq$30°	420 (11.1 ± 0.5 %)	251 (11.5 ± 0.7 %)	102 (10.1 ± 1.0 %)
	NGR	742	334	324
ETGs	ΔPA defined	301	204	97
	ΔPA $\geq$30°	84 (27.9 ± 2.6 %)	60 (29.4 ± 3.2 %)	24 (24.7 ± 4.4 %)
	NGR	231	140	91
S0 - Sas	ΔPA defined	677	483	194
	ΔPA $\geq$30°	66 (9.7 ± 1.1 %)	49 (10.1 ± 1.4 %)	17 (8.8 ± 2.0 %)
	NGR	100	44	56
Sb - Sds	ΔPA defined	1634	1112	522
	ΔPA $\geq$30°	88 (5.4 ± 0.6 %)	58 (5.2 ± 0.7 %)	30 (5.7 ± 1.0 %)
	NGR	107	32	75

aligned counterparts. This holds true for all morphologies. Chen et al. (2016) previously highlighted the boost in star formation in central regions for counter-rotating LTGs. As suggested, this could be a natural result of cancellation of angular momentum leading to increased in-flows to central regions. Our finding of lowered angular momentum in the counter-rotators (with respect to the co-rotators) supports this claim.

Due to the relationship between stellar mass, morphology, and specific angular momentum (e.g. Cortese et al. 2016), it might be expected that misaligned galaxies should be at higher stellar mass due to their lower λ_R with respect to the aligned (see also Bryant et al. 2019). Surprisingly for the overall population we see little difference, however, splitting on morphology as shown in Fig. 11 reveals individual trends. Misaligned ETGs (and NGRs) are more massive than the aligned counterparts most likely indicative that misaligned galaxies have had richer merger histories. The opposite trends are seen for both S0-Sas and Sb-Sds with kinematically aligned galaxies being of typically higher mass than the misaligned. This could be indicative that the pathways leading to misalignment are different as a function of morphology.

4.3 Group membership

Group membership is important for dictating the evolution of a galaxy and hence we now sub-divide our population into centrals and satellites as described in Section 2.7. Fig. 12 (top panels) shows the ΔPA distributions as in Fig. 10, but now split into centrals and satellites. Qualitatively the morphological trends remain however Table 2 reveals that centrals (29.4 ± 3.2 per cent) are slightly more likely to be misaligned than satellites (24.7 ± 4.4 per cent) for ETGs. This is also potentially seen for the S0-Sbs (10.1 ± 1.4 per cent for centrals versus 8.8 ± 2.0 per cent for satellites), however we note that both fractions are within each other's errorbars.

Fig. 13 shows the stellar mass distribution for our samples but now additionally split into centrals and satellites. Again we find the same qualitative trends for both centrals and satellites; i.e. misaligned ETGs are more massive than their aligned counterparts whereas misaligned S0-Sas and Sb-Sds are less massive than their aligned counterparts.

5 MISALIGNED GALAXIES IN TNG100

In this section, we utilize the mock sample created in TNG100 to interpret the properties of kinematically misaligned galaxies in MaNGA.

We divide our mock MaNGA sample based on the instantaneous star formation rate (SFR) of the galaxy. Here, we define SFR for all gas cells within twice the stellar half-mass radius of a given galaxy. The star forming main sequence for all galaxies is found by fitting a power law as a function of stellar mass. A galaxy is then flagged into one of three categories; star forming, green valley, or quenched depending on its deviation above or below the main sequence (Pillepich et al. 2019). The selected deviations from the main sequence are as follows; star forming galaxy: $\Delta \log_{10}(\mathrm{SFR}) > -0.5$, green valley galaxy: $-1.0 < \Delta \log_{10}(\mathrm{SFR}) < -0.5$, and quenched galaxy: $\Delta \log_{10}(\mathrm{SFR}) <= -1.0$.

The bottom panel of Fig. 12 shows the ΔPA distribution for the TNG100 sample split into centrals and satellites. Comparing to the observational sample in the top panel of Fig. 12, the morphological trends remain qualitatively the same with quenched/ETGs (star forming/LTGs) more likely to be misaligned (aligned).

Our choice to compare populations split on visual morphology in observations to SFR in simulations is one of necessity. The aim of this work is to explore the relationship of visual morphology with decoupled rotation. Unfortunately we do not currently have the equivalent classifications in IllustrisTNG100, so use an appropriate proxy. In future work, we will look at the relationship between observations and simulations using machine learning classifications of morphology, however, in the following subsections we follow the evolutionary history of the mock sample split by sSFR.

5.1 Angular momentum

In this subsection, we consider the angular momentum content of our TNG100 mock sample back to $z = 1$ for stars, gas, and dark matter individually. Angular momentum for our TNG100 galaxies is defined by the intrinsic specific angular momentum of their particles/cells:

$$\mathrm{j}_k = \frac{1}{\sum_n \mathrm{m}^{(n)}} \sum_n \mathrm{m}^{(n)} \boldsymbol{x}^{(n)} \times \boldsymbol{v}^{(n)}, \quad (3)$$

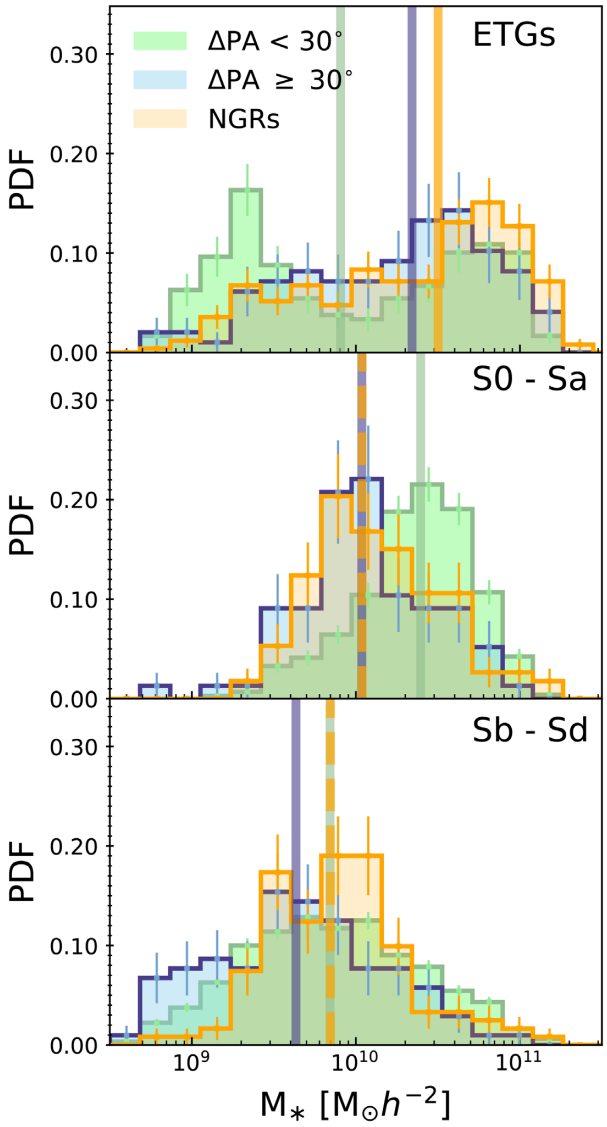

Figure 11. Probability density distributions of stellar mass, ($M_*/M_\odot$) for aligned galaxies ($\Delta PA < 30^\circ$), misaligned galaxies ($\Delta PA > 30^\circ$), and NGRs for ETGs, S0-Sas, and Sb-Sds (top to bottom). In each panel the aligned/misaligned are shown with solid lines with the aligned in the darker shade. NGRS are shown by dot-dashed lines. Each histogram is given with Poisson errors on each bin. The vertical lines denote the corresponding distribution's median. For ETGs, aligned galaxies are less massive than the misaligned sample. This trend, however, reverses for S0-Sas and Sb-Sds.

where $\boldsymbol{v}^{(n)}$ is the velocity of each particle relative to the centre of mass for the galaxy. $\boldsymbol{x}^{(n)}$ is the position of a given particle with respect to the position of the most gravitationally bound particle in the galaxy. We choose this definition since the centre of mass velocity can be biased by structure at large radii in the subhalo/galaxy and hence may spuriously not represent the true rotational centre. k is the particle/cell type referring to either stars, gas, or dark matter. For stars and gas this is calculated within a 3D radius equal to the 2D radius corresponding to the angular size of the mock observation. Dark matter is calculated for all particles assigned to the subhalo by the subfind algorithm.

Fig. 14 shows the specific angular momentum evolution from $z = 1$ for each of stars, gas, and DM split on group membership and morphology. We see that similar to the observational sample (see Section 4.1), misaligned galaxies in simulations are significantly lower stellar angular momentum than their aligned counterparts at $z = 0$. This is reflected in for each of stars, gas, and DM to various degrees for all morphologies and central/satellite definition. Interestingly, while misalignment between stars and gas may itself be a transient property, those misaligned at $z = 0$ reside in dark matter haloes with *fundamentally lower angular momentum* which persists to at least $z = 1$.

We note that particle based calculations of specific angular momentum scales with the number of particles. This results in more massive galaxies having higher j_i and further, quenched galaxies (that are typically more massive) having higher j_i than their later type counterparts. While there is only a small difference in-between the mass distributions of our aligned and misaligned samples, to ensure our signal is not simply driven by mass we calculate the residuals of j_{star} with respect to a typical galaxy of that mass. The residuals, Δj_{star} are calculated by fitting a polynomial to the distribution of j_{star} versus M_* for the galaxies (all mock observations, regardless if ΔPA is well defined) at each snapshot. Δj_{star}, is then defined as the deviation of a given galaxy away from the expectation of the fitted line at that mass. Since the trends are qualitatively consistent regardless of morphology, Fig. 15 shows the specific angular momentum residuals for the total population. For completeness we also include comparison to every galaxy in the mock sample (regardless if ΔPA is well defined). Misaligned galaxies ($\Delta PA \geq 30^\circ$) for both centrals and satellites show intrinsically lower Δj_{star} with respect to the total population at a given mass, indicative that it is not an effect due to mass. In addition, there is a relative evolution where Δj_{stars} diverges from all galaxies at $z \sim 0.5$ so that misaligned galaxies have even lower stellar angular momentum with respect to the aligned galaxies in recent times.

To conclude this section we now consider the directional 3D offsets between the angular momentum vectors of the stars, gas, and dark matter. These are calculated from:

$$\alpha_{3D} = \arccos\left(\frac{\boldsymbol{j}_i \cdot \boldsymbol{j}_j}{|\boldsymbol{j}_i|\,|\boldsymbol{j}_j|}\right), \tag{4}$$

where i, j refer to either stars, gas, or dark matter. As for the magnitudes of angular momentum, the star and gas vectors are calculated within a 3D radius set to that of the IFU footprint and the dark matter vector is calculated for all particles assigned to the subhalo by subfind. A comparison between calculating star–gas misalignment from angular momentum and from PA fitting can be found in Appendix A. Fig. 16 shows the evolution of the 3D offsets between each of stars, gas, and DM, respectively.

As expected splitting our sample on ΔPA results in significantly higher $\alpha_{STARS-GAS}$ at $z = 0$ for the misaligned galaxies found in the MaNGA observations. This is also typically correlated, albeit less strongly, with larger $\alpha_{STARS-DM}$ and α_{GAS-DM} at $z = 0$. This is indicative that a decoupling between stars and gas is often mirrored by a decoupling between the rotation of stars and DM. We also plot the average decoupling for all galaxies (all that are matched to MaNGA) between all components. In the middle panel, we see that $\alpha_{STARS-DM} \sim 50^\circ$ on average for all galaxies (gold line) with a slight redshift evolution which is roughly consistent with previous work (e.g. Chisari et al. 2017). We note that our choice to consider the direction of the star and gas rotation within the observational footprint is typically

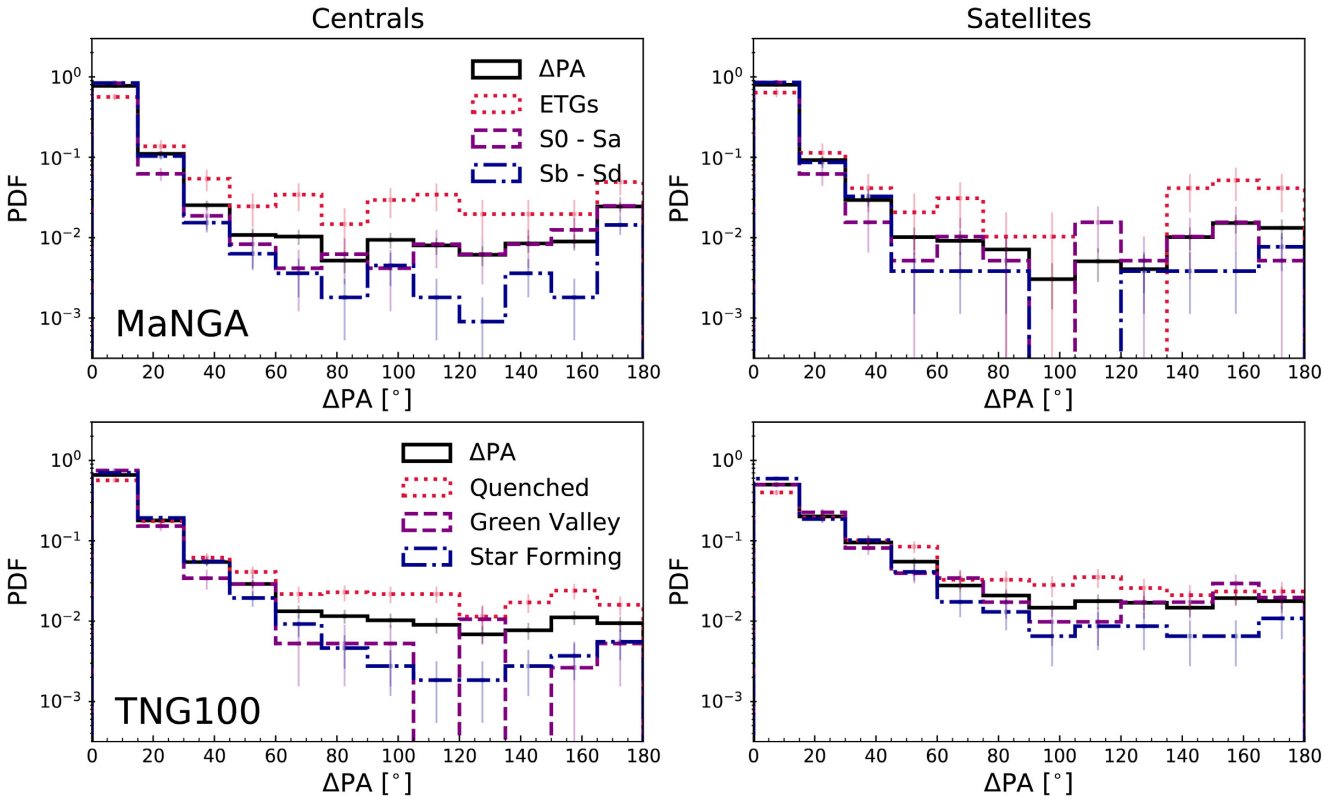

Figure 12. Same as Fig. 10, however split by group membership into centrals (left-hand panel) and satellites (right-hand panel). The top panel shows for the MaNGA sample and the bottom shows for the mock sample in TNG100. Morphology for TNG100 is categorized by the deviation of the galaxy's star formation away from the main sequence of galaxies in the whole of TNG100 (see Section 5).

far smaller than the overall DM halo, and hence, may lead to slightly higher typical misalignments between baryonic and DM components.

Working back from $z = 0$, we note that $\alpha_{\rm STARS-GAS}$ for the aligned and misaligned samples (selected at $z = 0$) converges in the majority of cases before $z = 1$. This indicates the transient nature of misalignment. This is in stark contrast to the magnitude of angular momentum for individual components (stars, gas, DM) which show a persistent difference in magnitude between aligned and misaligned objects (selected at $z = 0$) going back past at least $z = 1$.

6 DISCUSSION

In the previous sections we have demonstrated the relationship of kinematic misalignment with morphology, stellar angular momentum, and dark matter halo spin. In the following we put our results in context and highlight the potential of using the decoupling of star–gas rotation to identify underlying properties of a galaxy.

We note the close relationship of our findings of our samples with respect to the work of Starkenburg et al. (2019). They investigate the origin of star–gas decoupling (in this instance $>90^\circ$) using low mass galaxies (i.e. $2 \times 10^9 < M_* < 5 \times 10^{10}$) in the original Illustris simulation. Despite extending the mass range and only considering the ensemble average for aligned and misaligned galaxies split at ΔPA=30°, we still find the same qualitative trends of lower angular momentum and lower gas mass fractions for misaligned galaxies (in comparison to aligned).

While outside the scope of this work, we note that their estimation of relaxation time-scales (i.e. until realignment of rotation axes) is of the order of Gigayears. This appears to be roughly comparable to toy-model estimates (see Davis & Bureau 2016, albeit for ETGs). Here we also demonstrate the transient nature of star–gas decoupling (left-hand panels, Fig. 16). Working back from $z = 0$, we note that $\alpha_{\rm STARS-GAS}$ for the aligned and misaligned samples (at $z = 0$) converges in the majority of cases before $z = 1$. Since we are only considering the ensemble average for misalignment selected at $z = 0$, we cannot comment on the time-scales of misalignment here since the average may include several events that decouple the rotation.

In contrast, we see that the magnitude of specific angular momentum for stars, gas, and DM for misaligned objects (at $z = 0$) remains fundamentally lower going to at least $z = 1$. This suggests that while star–gas misalignment at $z = 0$ is a transient property, *its likelihood is correlated with the angular momentum content of the halo at early times*. In part, the correlation must be driven by the lower angular momentum content of the stellar component. This inherently leads to longer relaxation time-scales (i.e. longer star–gas decoupling) due to weaker stellar torques acting on the misaligned gas component and hence a higher likelihood of being misaligned at $z = 0$.

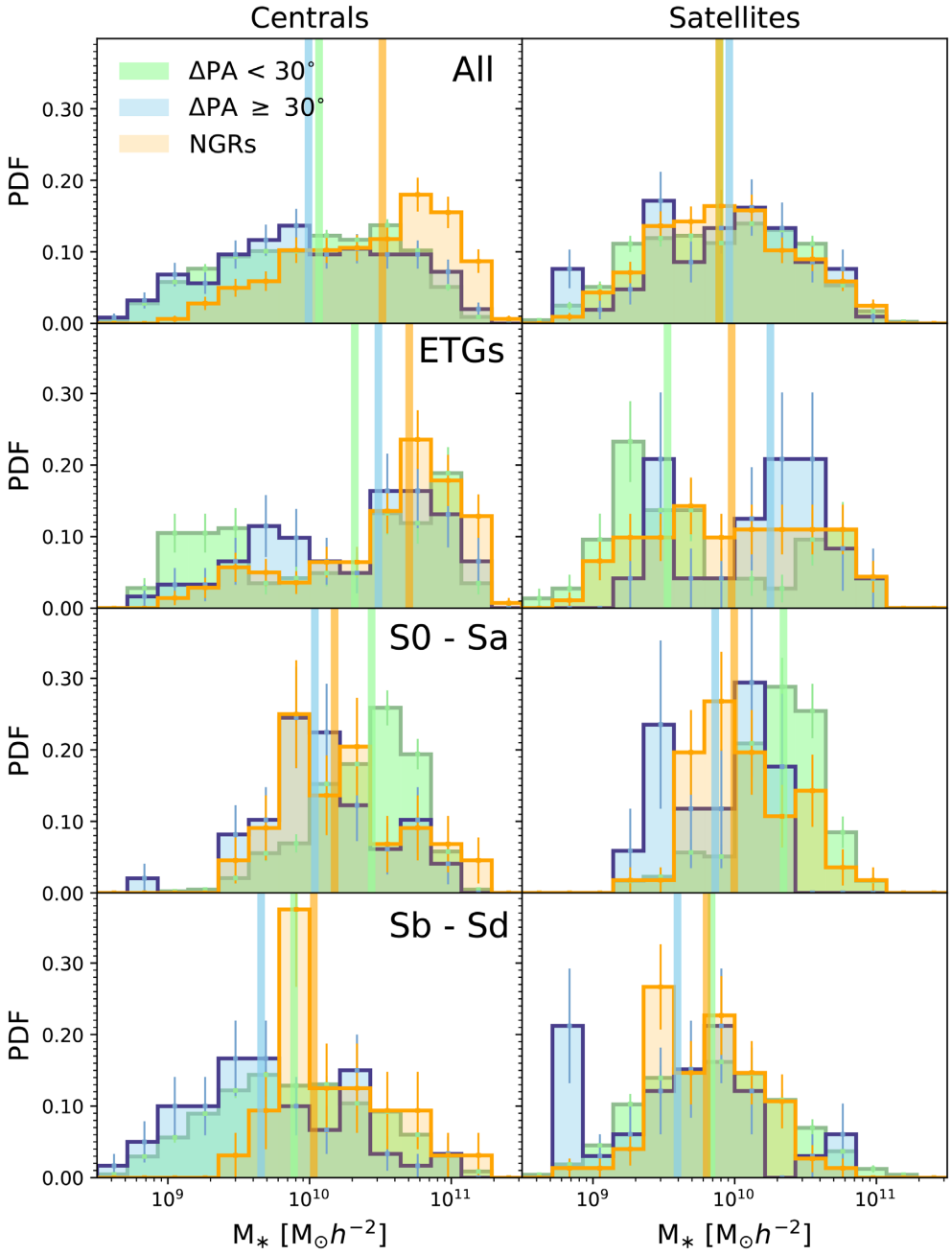

Figure 13. Same as Fig. 11, however split by group membership into centrals (left-hand panel) and satellites (right-hand panel). Additionally the distributions for the overall central and satellite populations is shown in the top row. We see that for ETGs there is a strong difference in mass between aligned and misaligned satellites. This trend is reversed for S0/Sa and Sb/Sd satellites. These trends are also seen for centrals, however, typically to a lesser degree.

We note the apparent relationship of misalignment with the different evolution of low and high spin haloes due to environment. In Horizon-AGN, Khim et al. (2019) show that the misalignment fraction strongly increases in cluster environments. While not explicitly shown in this work, we find that misaligned satellites are typically closer to group centres, indicating the importance of gas stripping or interactions. In observations, Li et al. (2019) find that at least 40 per cent of misalignment can be attributed to recent mergers or interactions. The environment of a given galaxy, modulating the probability of mergers/interactions and hence the spin of the halo/galaxy appears to be an important factor in dictating the misalignment fraction. However, current studies of the environmental dependence of misalignment in observations are inconclusive (e.g. preference for misalignment in overdensity versus isolation; Jin et al. 2016; Duckworth et al. 2019b).

We also note TNG100's ability to not only reproduce a reasonable distribution of ΔPA with respect to the MaNGA sample (Fig. 5) once accounting for variances in mass between the ΔPA defined samples in MaNGA and TNG100, but also reproduc-

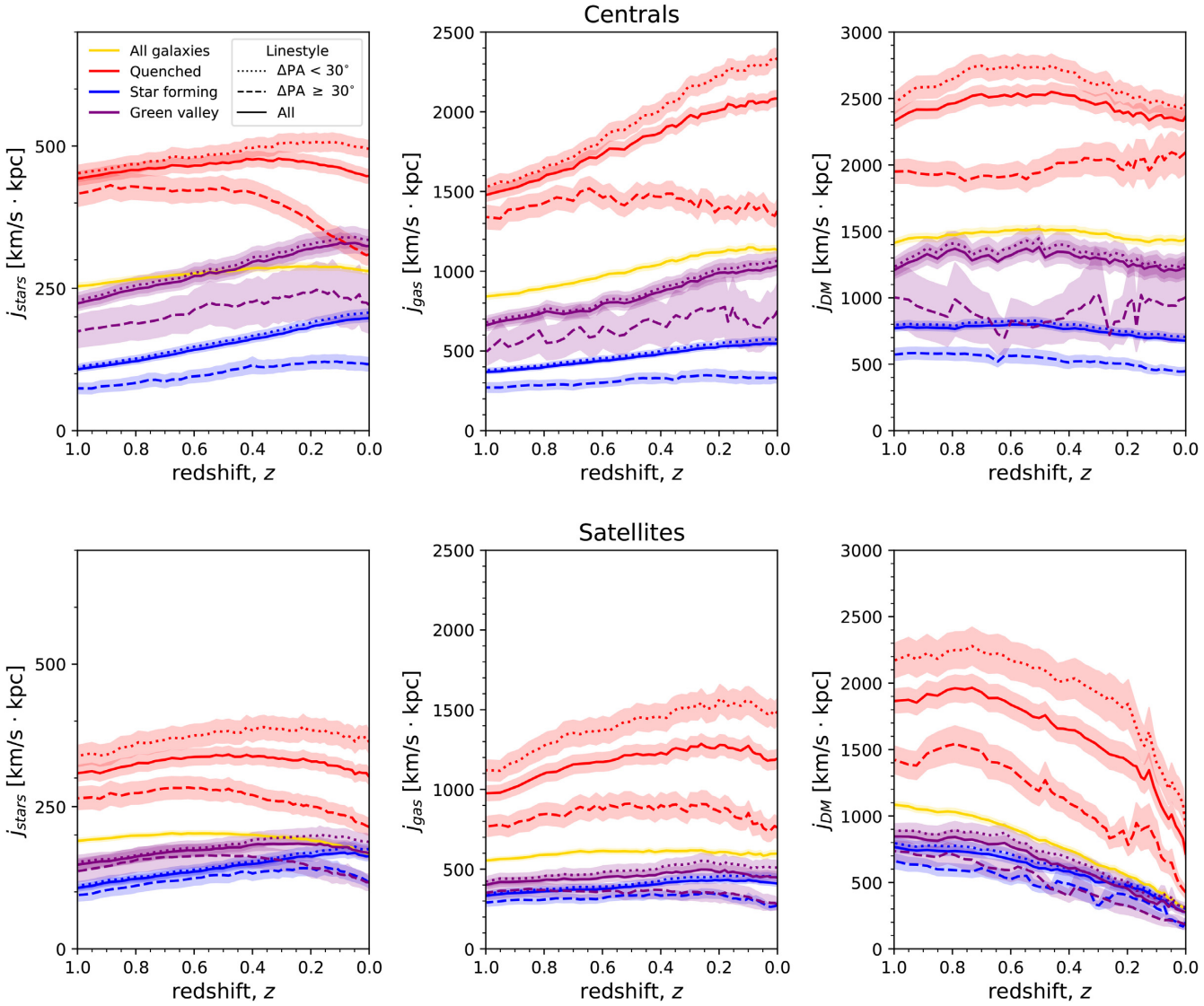

Figure 14. Specific angular momentum evolution from $z = 1$ calculated from star, gas, and DM particles (left to right). The angular momentum is calculated for all star and gas particles/cells within the 3D radius assigned by the mock IFU observation, whereas DM is found from all particles associated to the subhalo. The evolution is taken as the median at each time-step for all galaxies of that category with errorbars showing the standard error. The top (bottom) row shows the evolution for central (satellite) galaxies. Each panel displays the evolution split into morphologies; quenched (red), green valley (purple), and star forming (blue) and also ΔPA $<30^\circ$ (dotted) and $>30^\circ$ (dashed). Kinematically misaligned galaxies selected at $z = 0$ have notably lower specific angular momentum for all of stars, gas, and dark matter.

ing the strong trends with morphology found in observations (Fig. 12).

Whether the trigger of misalignment is internal or external, it appears to be clearly linked to a lowered gas mass (Fig. 9). In future work we will use our observational and simulated samples to break down the prevalence of driving factors.

7 CONCLUSION

In this work, we introduce a catalogue of ∼4500 galaxies from the MaNGA survey in order to establish the prevalence of misalignment as a function of morphology and angular momentum. We also construct a mock MaNGA sample in IllustrisTNG100 to determine the time evolution of angular momentum in star–gas decoupled galaxies and their relationship with halo spin. Our conclusions are as follows:

(i) (MaNGA) The prevalence of kinematic misalignment (i.e. where rotational axes of stars and gas are offset by $>30^\circ$) is strongly morphological dependent with ETGs having ∼28 per cent exhibiting misalignment which decreases to ∼5 per cent for Sb-Sds.

(ii) (MaNGA) For all morphologies this misalignment is related to a lowered stellar angular momentum and also a lowered gas mass. We note that misaligned galaxies have similar stellar angular momentum to those do not have coherently rotating gas (those with large gas depletion fall into this category). This

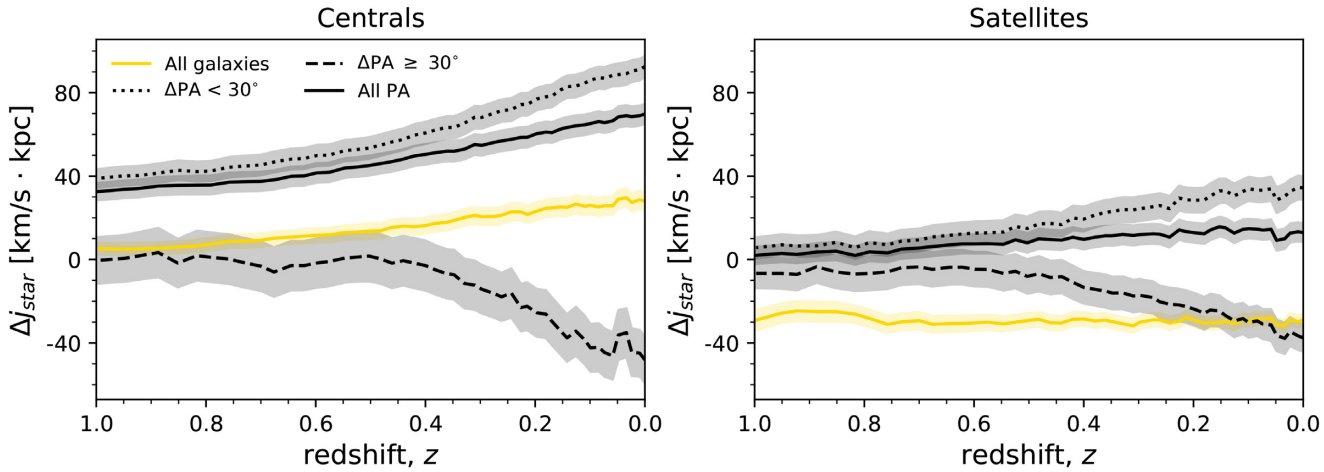

Figure 15. The specific angular momentum residuals from $z = 1$ for all star particles within the 3D radius assigned by the mock IFU observation. The residual is calculated as the deviation away from the expectation for a galaxy of that mass at each snapshot. The evolution of the residual is taken as the median at each time-step for all galaxies of that category with errorbars showing the standard error. The right (left)-hand panel shows the evolution for central (satellite) galaxies. Each panel displays the evolution for all galaxies (yellow), of which have a defined ΔPA (black solid), aligned galaxies ΔPA $<30^\circ$ (black dotted) and misaligned $>30^\circ$ (black dashed). We see that the difference in angular momentum between aligned and misaligned galaxies is not due to differences in mass. In addition we note a marked deviation of misaligned galaxies to even lower angular momentum in recent times.

could be indicative that galaxies without coherent gas rotation and kinematically misaligned galaxies are different time-steps in the same evolutionary sequence. As noted in simulations (van de Voort et al. 2015; Starkenburg et al. 2019), a key component in decoupling star–gas rotation is a significant gas loss followed by accretion of new gas with misaligned angular momentum. In this scenario, NGRs could represent an earlier timestamp before a future re-accretion of gas. This would indicate that the stellar angular momentum is disrupted prior to accretion of new material.

(iii) (MaNGA) We find that the misalignment fraction is also dependent on group membership. For ETGs and S0-Sas, central galaxies are more likely to exhibit misalignment than satellites. For Sb-Sds this trend reverses.

(iv) (MaNGA) We find that counter-rotation (i.e. rotational axes of stars and gas are offset by $>150^\circ$) is a stable state for galaxies of all morphologies shown by a boost in the PDF (Fig. 10). Similar to the total misaligned population, counter-rotators have distinctly lower angular momentum than their aligned counterparts.

(v) (IllustrisTNG100) We find that a mock MaNGA like sample constructed from cosmological scale hydrodynamical simulation IllustrisTNG100 reproduces the observed trends of decoupling with morphology and stellar angular momentum at $z = 0$.

(vi) (IllustrisTNG100) We find that decoupled galaxies reside in dark matter haloes with lower spin going back past $z = 1$. Despite the decoupling between gas and stars being inherently transient in nature, it is also associated with a decoupling of both stars and gas with respect to dark matter. This demonstrates the inherent link of decoupling, not only to present-day stellar angular momentum, but to lower spin haloes at $z = 1$.

In the second paper of this series we use our simulated sample to investigate the temporal connection between black hole activity and misalignment (Duckworth et al. 2019a). In the future, we will investigate the typical time-scales and origins of misalignment and merger rates in ETGs.

ACKNOWLEDGEMENTS

CD acknowledges support from the Science and Technology Funding Council (STFC) via an PhD studentship (grant number ST/N504427/1). The Flatiron Institute is supported by the Simons Foundation.

We thank the IllustrisTNG team for help and data access. While this work was conducted using the public data release, it would have not been possible without their help and use of the IllustrisTNG private data for the purposes of other research works.

SDSS-IV is managed by the Astrophysical Research Consortium for the Participating Institutions of the SDSS Collaboration including the Brazilian Participation Group, the Carnegie Institution for Science, Carnegie Mellon University, the Chilean Participation Group, the French Participation Group, Harvard-Smithsonian Center for Astrophysics, Instituto de Astrofísica de Canarias, The Johns Hopkins University, Kavli Institute for the Physics and Mathematics of the Universe (IPMU) / University of Tokyo, Lawrence Berkeley National Laboratory, Leibniz Institut für Astrophysik Potsdam (AIP), Max-Planck-Institut für Astronomie (MPIA Heidelberg), Max-Planck-Institut für Astrophysik (MPA Garching), Max-Planck-Institut für Extraterrestrische Physik (MPE), National Astronomical Observatory of China, New Mexico State University, New York University, University of Notre Dame, Observatório Nacional / Ministry of Science and Techology of Brazil (MCTI), The Ohio State University, Pennsylvania State University, Shanghai Astronomical Observatory, United Kingdom Participation Group, Universidad Nacional Autónoma de México, University of Arizona, University of Colorado Boulder, University of Oxford, University of Portsmouth, University of Utah, University of Virginia, University of Washington, University of Wisconsin, Vanderbilt University, and Yale University.

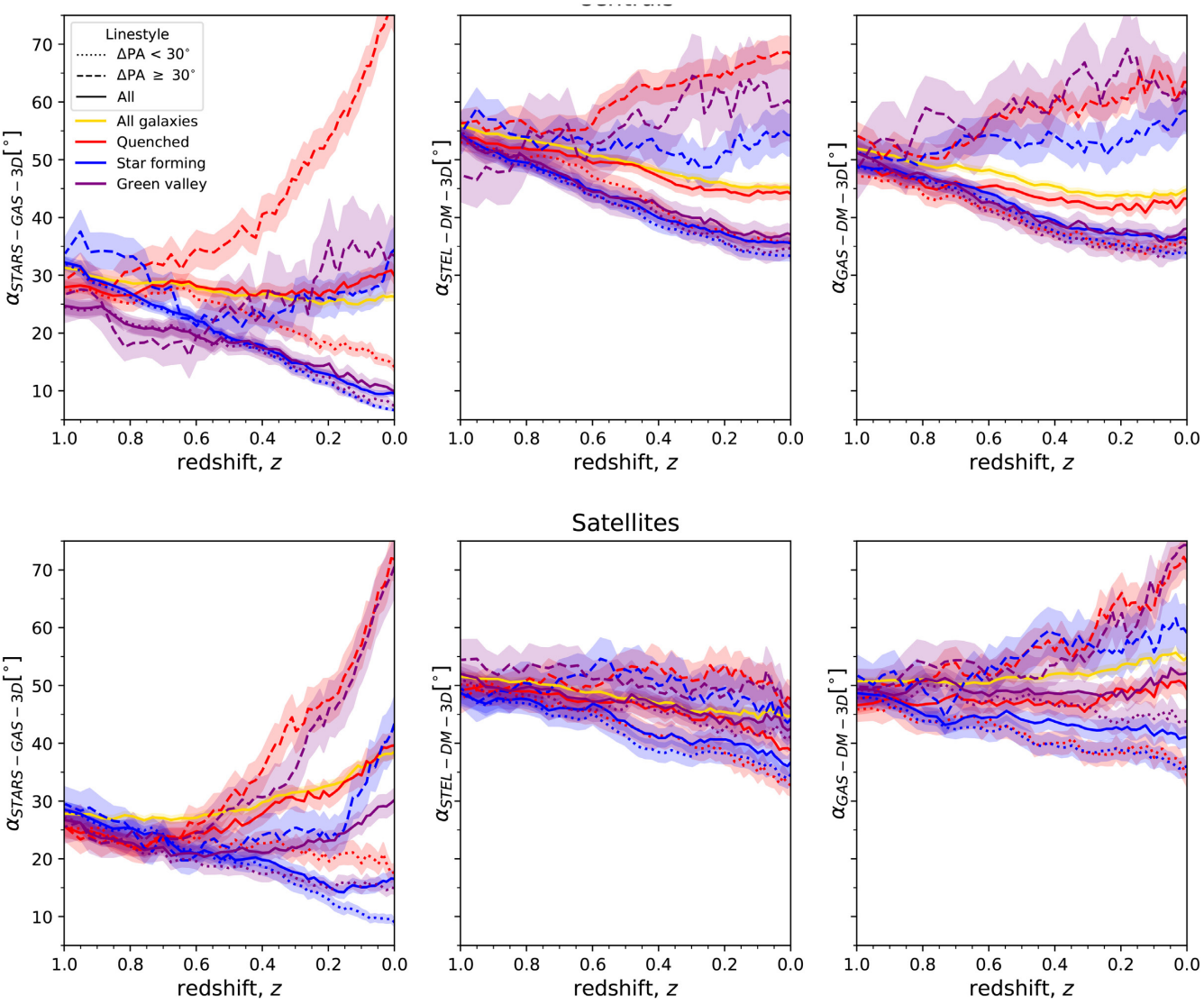

Figure 16. Evolution of the 3D offset (in degrees) between the principal spin axes of; stars and gas (left-hand panel), stars and dark matter (middle), and gas and dark matter (right-hand panel) from $z = 1$. The evolution is taken as the median at each time-step for all galaxies of that category with errorbars showing the standard error. The top (bottom) row shows the evolution for central (satellite) galaxies. Each panel displays the evolution split into morphologies; quenched (red), green valley (purple), and star forming (blue) and also ΔPA $<30^\circ$ (dotted) and $\geq 30^\circ$ (dashed).

REFERENCES

Arnold J. A. et al., 2014, ApJ, 791, 80
Bacon R. et al., 2001, MNRAS, 326, 23
Barrera-Ballesteros J. K. et al., 2014, A&A, 568, A70
Barrera-Ballesteros J. K. et al., 2015, A&A, 582, A21
Barrera-Ballesteros J. K. et al., 2018, ApJ, 852, 74
Belfiore F. et al., 2019, AJ , 158, 160
Blanton M. R., Kazin E., Muna D., Weaver B. A., Price-Whelan A., 2011, AJ, 142, 31
Blanton M. R. et al., 2017, AJ, 154, 28
Bryant J. J. et al., 2015, MNRAS, 447, 2857
Bryant J. J. et al., 2019, MNRAS, 483, 458
Bundy K. et al., 2015, ApJ, 798, 7
Cappellari M., Copin Y., 2003, MNRAS, 342, 345
Cappellari M., Emsellem E., 2004, PASP, 116, 138
Cappellari M. et al., 2011, MNRAS, 413, 813
Cappellari M., 2017, MNRAS, 466, 798
Chen Y.-M. et al., 2016, Nat. Commun., 7, 13269
Chisari N. E. et al., 2017, MNRAS, 472, 1163
Codis S., Pichon C., Pogosyan D., 2015, MNRAS, 452, 3369
Conroy C., Gunn J. E., 2010, ApJ, 712, 833
Conroy C., Gunn J. E., White M., 2009, ApJ, 699, 486
Cortese L. et al., 2016, MNRAS, 463, 170
Croom S. M. et al., 2012, MNRAS, 421, 872
Davis M., Efstathiou G., Frenk C. S., White S. D. M., 1985, ApJ, 292, 371
Davis T. A., Bureau M., 2016, MNRAS, 457, 272
Davis T. A. et al., 2011, MNRAS, 417, 882
Davis T. A. et al., 2013, MNRAS, 429, 534
Doroshkevich A. G., 1970, Astrophysics, 6, 320
Drory N. et al., 2015, AJ, 149, 77
Duckworth C., Starkenburg T. K., Genel S., Davis T., Habouzit M., Kraljic K., Tojeiro R., 2019a, preprint (arXiv:1911.05091)
Duckworth C., Tojeiro R., Kraljic K., Sgró M. A., Wild V., Weijmans A.-M., Lacerna I., Drory N., 2019b, MNRAS, 483, 172
Emsellem E. et al., 2007, MNRAS, 379, 401
Emsellem E. et al., 2011, MNRAS, 414, 888

Falcón-Barroso J., Sánchez-Blázquez P., Vazdekis A., Ricciardelli E., Cardiel N., Cenarro A. J., Gorgas J., Peletier R. F., 2011, A&A, 532, A95
Fall S. M., Efstathiou G., 1980, MNRAS, 193, 189
Foreman-Mackey D., Sick J., Johnson B., 2014, python-fsps: Python bindings to FSPS (v0.1.1). Available at: https://doi.org/10.5281/zenodo.12157
Foster C., Arnold J. A., Forbes D. A., Pastorello N., Romanowsky A. J., Spitler L. R., Strader J., Brodie J. P., 2013, MNRAS, 435, 3587
Genel S., Fall S. M., Hernquist L., Vogelsberger M., Snyder G. F., Rodriguez-Gomez V., Sijacki D., Springel V., 2015, ApJ, 804, L40
Genel S. et al., 2018, MNRAS, 474, 3976
Graham M. T. et al., 2018, MNRAS, 477, 4711
Gunn J. E. et al., 2006, AJ, 131, 2332
Hoyle F., 1951, Proc. Symp., Motion of Gaseous Masses of Cosmical Dimensions. Problems of Cosmical Aerodynamics. International Astronomical Union and International Union of Theoretical and Applied Mechanics, UNESCO, p. 195
Jin Y. et al., 2016, MNRAS, 463, 913
Khim D. J. et al., 2019, preprint (arXiv:1911.06825)
Krajnović D., Cappellari M., de Zeeuw P. T., Copin Y., 2006, MNRAS, 366, 787
Lagos C. d. P., Padilla N. D., Davis T. A., Lacey C. G., Baugh C. M., Gonzalez-Perez V., Zwaan M. A., Contreras S., 2015, MNRAS, 448, 1271
Lagos C. d. P., Theuns T., Stevens A. R. H., Cortese L., Padilla N. D., Davis T. A., Contreras S., Croton D., 2017, MNRAS, 464, 3850
Lagos C. d. P. et al., 2018, MNRAS, 473, 4956
Laigle C. et al., 2015, MNRAS, 446, 2744
Law D. R. et al., 2015, AJ, 150, 19
Law D. R. et al., 2016, AJ, 152, 83
Li S.-l. et al., 2019, preprint (arXiv:1912.04522)
Lim S. H., Mo H. J., Lu Y., Wang H., Yang X., 2017, MNRAS, 470, 2982
Marinacci F. et al., 2018, MNRAS, 480, 5113
Mo H. J., Mao S., White S. D. M., 1998, MNRAS, 295, 319
Naiman J. P. et al., 2018, MNRAS, 477, 1206
Nair P. B., Abraham R. G., 2010, ApJS, 186, 427
Nelson D. et al., 2018, MNRAS, 475, 624
Nelson D. et al., 2019, Comput. Astrophys. Cosmol., 6, 2
Pakmor R., Springel V., 2013, MNRAS, 432, 176
Pakmor R., Bauer A., Springel V., 2011, MNRAS, 418, 1392
Peebles P. J. E., 1969, ApJ, 155, 393
Pichon C., Pogosyan D., Kimm T., Slyz A., Devriendt J., Dubois Y., 2011, MNRAS, 418, 2493
Pillepich A. et al., 2018a, MNRAS, 473, 4077
Pillepich A. et al., 2018b, MNRAS, 475, 648
Pillepich A. et al., 2019, MNRAS, 490, 3196
Sánchez S. F. et al., 2016, Rev. Mex. Astron. Astrofis., 52, 171
Sánchez S. F. et al., 2018, Rev. Mex. Astron. Astrofis., 54, 217
Sánchez-Blázquez P. et al., 2006, MNRAS, 371, 703
Smee S. A. et al., 2013, AJ, 146, 32
Springel V., 2010, MNRAS, 401, 791
Springel V., White S. D. M., Tormen G., Kauffmann G., 2001, MNRAS, 328, 726
Springel V. et al., 2018, MNRAS, 475, 676
Stark D. V. et al., 2018, MNRAS, 480, 2217
Starkenburg T. K., Sales L. V., Genel S., Manzano-King C., Canalizo G., Hernquist L., 2019, ApJ, 878, 143
van de Voort F., Davis T. A., Kereš D., Quataert E., Faucher-Giguère C.-A., Hopkins P. F., 2015, MNRAS, 451, 3269
Weinberger R. et al., 2017, MNRAS, 465, 3291
Westfall K. B. et al., 2019, AJ , 158, 231
White S. D. M., Rees M. J., 1978, MNRAS, 183, 341
Willett K. W. et al., 2013, MNRAS, 435, 2835
Yan R. et al., 2016a, AJ, 151, 8
Yan R. et al., 2016b, AJ, 152, 197
Yang X., Mo H. J., van den Bosch F. C., Jing Y. P., 2005, MNRAS, 356, 1293
Yang X., Mo H. J., van den Bosch F. C., Pasquali A., Li C., Barden M., 2007, ApJ, 671, 153

APPENDIX: PA VERSUS ABSOLUTE OFFSET

A key assumption of this work is the ability for the projected ΔPA to be a reliable estimator of the actual 3D offset between star and gas rotation axes. Fig. A1 shows the distributions of the difference between ΔPA and the 2D and 3D offsets between the angular momentum principal axes of stars and gas. See equation (4) for calculation of the 3D offset; the 2D equivalent is simply a projection of this on to the XY plane. ΔPA is a reasonable measure of the true 3D offset which can be modelled as a Gaussian centred on 0° with a standard deviation of 17.6° (green dotted line). The deviation of the 2D projection from the true 3D offset (black line) has a standard deviation of 13°, demonstrating that the variation is both due to projection and the noise associated with observations. Additionally, we note the different particle selection for the two measures which may drive slight differences. While the 2D/3D offsets and ΔPA are measured in a footprint with the same radius, the offsets are only defined for particles within a 3D sphere of this radius, where ΔPA is defined for all particles along the line of sight enclosed by the sky footprint.

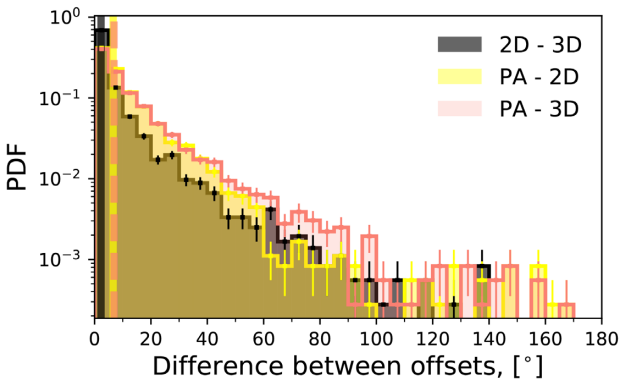

Figure A1. Probability density distribution of the difference between various measures of the star–gas rotational angle offset. The difference between the 3D angular momentum vectors and projection in 2D is shown (black), ΔPA and 2D (yellow) and ΔPA and 3D (red).

This paper has been typeset from a TEX/LATEX file prepared by the author.